Lab on a Chip

TUTORIAL REVIEW

View Article Online
View Journal | View Issue

Cite this: *Lab Chip*, 2022, **22**, 1254

Technologies for measuring red blood cell deformability

Kerryn Matthews, [ab] Erik S. Lamoureux,[ab] Marie-Eve Myrand-Lapierre,[a] Simon P. Duffy[bc] and Hongshen Ma *[abde]

Human red blood cells (RBCs) are approximately 8 μm in diameter, but must repeatedly deform through capillaries as small as 2 μm in order to deliver oxygen to all parts of the body. The loss of this capability is associated with the pathology of many diseases, and is therefore a potential biomarker for disease status and treatment efficacy. Measuring RBC deformability is a difficult problem because of the minute forces (~pN) that must be exerted on these cells, as well as the requirements for throughput and multiplexing. The development of technologies for measuring RBC deformability date back to the 1960s with the development of micropipette aspiration, ektacytometry, and the cell transit analyzer. In the past 10 years, significant progress has been made using microfluidics by leveraging the ability to precisely control fluid flow through microstructures at the size scale of individual RBCs. These technologies have now surpassed traditional methods in terms of sensitivity, throughput, consistency, and ease of use. As a result, these efforts are beginning to move beyond feasibility studies and into applications to enable biomedical discoveries. In this review, we provide an overview of both traditional and microfluidic techniques for measuring RBC deformability. We discuss the capabilities of each technique and compare their sensitivity, throughput, and robustness in measuring bulk and single-cell RBC deformability. Finally, we discuss how these tools could be used to measure changes in RBC deformability in the context of various applications including pathologies caused by malaria and hemoglobinopathies, as well as degradation during storage in blood bags prior to blood transfusions.

Received 23rd November 2021,
Accepted 28th February 2022

DOI: 10.1039/d1lc01058a

rsc.li/loc

1. Introduction

Red blood cells (RBCs) are discoid shaped anuclear cells, measuring 6–8 μm in diameter and 2–3 μm in thickness. To perform their function of delivering oxygen from the lungs to all the tissues of our body, RBCs must fit through capillaries less than half their diameter.[1] Their ability to squeeze through capillaries is made possible by the extraordinary ability of RBCs to deform. Deformability is primarily determined by the intracellular viscosity (hemoglobin content and structure), as well as membrane flexibility/rigidity of the RBC. As RBCs age during their normal lifespan of 100–120 days, they gradually lose the ability to deform, causing their sequestration by inter-endothelial clefts (0.5–1 μm) in the spleen and ultimately their destruction by splenic macrophages that remove them from the circulation.[1–4] The destroyed RBCs are continuously replaced by new RBCs made in the bone marrow, which maintains a consistent average deformability of the overall RBC population.

In addition to natural aging, the loss of RBC deformability has been associated with the pathology of many diseases, including malaria,[5–8] hemoglobinopathies such as thalassemia[9–13] and sickle cell disease,[14–16] and diabetes.[17–19] Therefore, changes in RBC deformability provide a potential physical biomarker for disease diagnosis and monitoring treatment efficacy. As a result, there have been efforts to develop technologies for measuring RBC deformability since the 1960s, due to the key challenge of accurately measuring or applying the minute forces (~pN) that are required for deforming single RBCs.[20] Furthermore, the use of RBC deformability in biological assays is also limited by the difficulty in discriminating a small fraction of abnormal RBCs from the vast numbers of normal RBCs.

Traditional techniques for measuring RBC deformability can be divided into bulk flow and single-cell methods. Bulk flow methods, such as ektacytometry[21–23] and micropore filtration,[24–26] provide a measure of the average deformability

[a] *Department of Mechanical Engineering, University of British Columbia, 2054-6250 Applied Science Lane, Vancouver, BC, V6T 1Z4, Canada.*
E-mail: hongma@mech.ubc.ca
[b] *Centre for Blood Research, University of British Columbia, Vancouver, BC, Canada*
[c] *British Columbia Institute of Technology, Vancouver, BC, Canada*
[d] *Department of Urologic Science, University of British Columbia, Vancouver, BC, Canada*
[e] *Vancouver Prostate Centre, Vancouver General Hospital, Vancouver, BC, Canada*

of thousands of cells. Single-cell techniques, such as atomic force microscopy,[12,27] optical tweezers,[28–30] and micropipette aspiration[31,8,32] allow for the precise measurement of a few individual cells with low throughput. Recent advances in microfluidics have produced several new methods for measuring RBC deformability including wedging in tapered constrictions,[33,34] elongation *via* fluid shear stress,[35,36] deformation *via* extensional flows,[37–40] pressure drop while transiting constrictions,[41] impedance,[42] transit pressure through microscale constrictions,[5] transit time through microscale constrictions[43,44] and sorting RBC based on deformability for further downstream analysis.[45,46]

In this review, we provide an overview of both traditional and microfluidic techniques and compare their sensitivity and throughput in measuring both bulk and single RBC deformability. We define sensitivity as the ability to distinguish RBCs treated with mild glutaraldehyde (GTA) fixation from control. GTA induces cross-linking of RBC membrane proteins, which when used at very low concentrations, could induce concentration-dependent loss of RBC deformability. In addition to sensitivity and throughput, we discuss the usability of each tool and evaluate each for its robustness against clogging by rigid RBCs or RBC aggregates. Finally, we discuss how RBC deformability assessment can be applied in various health contexts including transfusion medicine, malaria, hemoglobinopathies, and diabetes.

2. Traditional bulk flow techniques

Bulk flow methods measure the deformability of thousands of cells in a bulk RBC sample. These techniques measure the average deformability of a cell sample, but they are unable to detect deformability changes in a small fraction of abnormal cells in a sample containing primarily normal RBCs.

2.1 Ektacytometry

Ektacytometry provides a measure of the average RBC deformability in response to changes in shear stress. RBCs are suspended in a viscous medium and introduced into a gap between two rotating surfaces that applies shear stress to the RBC suspension. The resulting aggregate change in cell elongation due to shear is detected using a laser beam directed through the suspension, creating a diffraction pattern (Fig. 1A).[21–23,47] The rotating apparatuses used to make ektacytometers include the Couette and parallel disk systems. In the Couette system, the RBC suspension is contained between a stationary cylinder and a rotating cylinder (Fig. 1A).[48,49] In the parallel disk system, the RBC suspension is confined between stationary and rotating disks (Fig. 1B).[50] Under shear stress, the RBCs elongate and align with the fluid streamlines in the laminar shear flow. The ellipticity of the diffraction pattern changes based on the degree of deformation. The shape of the ellipse characterizes the average deformability of the RBCs and is expressed as the elongation index (EI, eqn (1)), where the length of the long axis (L) and the length of the short axis (W) is from the elliptical diffraction pattern (Fig. 1A).[48]

$$\mathrm{EI} = \frac{(L - W)}{(L + W)} \tag{1}$$

Ektacytometry provides a measure of the average deformability of a suspension of cells and is not affected by the presence of RBC aggregates or differences in cell size. Ektacytometry has been used to sensitively distinguish the deformability of 0.001% GTA-treated RBCs from control RBCs.[22] However, this technique obscures information on subpopulations of diseased cells (<10%) that form part of the overall population, such as in cases of *P. falciparum* infection.[51] Where ektacytometry has been used in the study of parasitized RBCs, the measured loss of RBC deformability resulted from the rigidification of the uninfected RBCs (typically >99% of the population) and not due to the rigidification of the infected RBC (typically <1% of the population).[52,53] Ektacytometry has been used to study RBC deformability changes in bulk RBC samples from patients with hemoglobinopathies, such as sickle cell anemia,[10,11,54–58] diabetes,[59] as well as during storage in

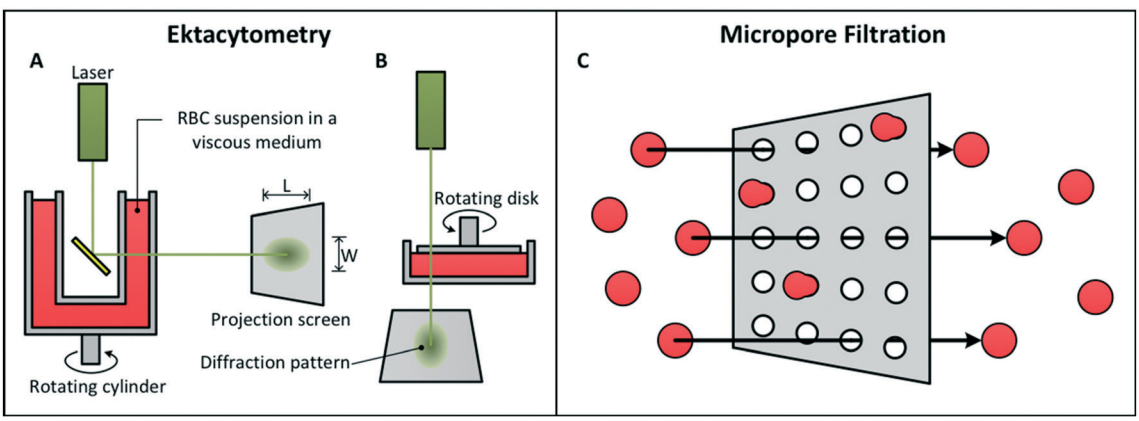

Fig. 1 Bulk flow techniques – ektacytometry and micropore filtration. Principle of the (A) Couette and (B) parallel disk ektacytometry systems. (C) Principle of micropore filtration.

blood bags,[60] but was unable to quantify the abundance of subpopulations of rigid RBCs in a sample. Ektacytometry has been upgraded in several ways, including the laser optical rotational red cell analyzer (LoRRca) system[61] or Laser-assisted optional rotational cell analyzer (LORCA),[62] which measures RBC shear stress in various osmolarity gradients, as well as the LoRRca MaxSis that combines RBC ektacytometry with an osmotic gradient and aggregometry. The oxygenscan (pO_2scan) further augments the LoRRca system by enabling the measurement of RBC deformability as a function of a continuously changing gradient of O_2 tension. These upgrades have mostly been used in studies of sickle cell disease.[63–66] In addition, this technique has been translated to a microfluidic platform that has been commercialized as the RheoSCAN.[47,67] This microfluidic ektacytometer passes a 5 μl sample through a microfluidic channel and laser diffraction is used to evaluate RBC shape in as little as 1–2 min. This microfluidic rheometry technique can discriminate between red blood cells stiffened in glutaraldehyde concentrations of 0, 0.3, 0.5, and 1.0 mM (0.001–0.02%), and is in excellent agreement with the conventional ektacytometers and LORCA.[47,61]

2.2 Micropore filtration

Micropore filtration measures RBC deformability using a polycarbonate membrane filter with pores smaller than the diameter of RBCs (Fig. 1C).[24–26] The RBC sample is pushed through the membrane filter at a fixed flow rate from a syringe pump. Poorly deformable RBCs require longer time to cross the filter than highly deformable RBCs. The transit time for the RBC sample to cross the filter defines the average deformability, which is expressed as the deformability index (DI). The DI is calculated from the volume of the blood sample processed (V), the hematocrit (hct) of the blood samples, and the time, in minutes, needed to filter the whole sample (eqn (2)).[24] A dimensionless value could also be obtained by processing 1 ml of blood. In this case, eqn (2) is divided by 1 ml and multiplied by the equivalent of one minute.[25]

$$\mathrm{DI} = \frac{V \times hct}{\mathrm{time}} \tag{2}$$

Micropore filtration had been a popular technique because of its simplicity. However, the sensitivity of this technique is low, as it can only distinguish between 0.04% (ref. 68) and 0.0125% (ref. 69) GTA-treated and control RBCs. Furthermore, white blood cells and platelets reduce the filtration rate since they tend to be trapped and therefore clog the membrane filter and have a great impact on DI measurements.[51,70] Samples therefore require additional processing to remove these cells from the RBC population prior to filtration. Subpopulations of RBCs also cannot be measured or quantified using micropore filtration. This technology has been used to study the bulk RBC deformability changes in the case of hemoglobinopathies[13,71] and during storage in blood bags,[25] and is more recently used as a comparison technique for novel microfluidics assays due to its low sensitivity.[68,72]

3. Traditional single-cell techniques

Unlike bulk flow methods; single cells techniques allow the measurement of subpopulations of RBCs within a sample by measuring the deformability of individual RBCs. Key metrics for assessing single cell techniques are throughput, sensitivity, repeatability, and ease-of-use.

3.1 Micropipette aspiration (MPA)

Another early approach for measuring single cell RBC deformability is micropipette aspiration, which has been used to study cell biomechanics for more than 50 years. MPA measures the extensional rigidity (also known as the shear modulus, μ) of individual RBCs, which is calculated from the uniaxial elongation or shear deformation of the RBC membrane.[31,8,32,73] Micropipette aspiration studies of RBCs are performed by suctioning individual RBCs partially or completely into a glass micropipette with an internal radius (R_p) smaller than the radius of the RBC (Fig. 2A). When RBCs are partially suctioned into the micropipette, the relationship between the suction pressure (P) and the length of the protrusion (L) is used to determine the intrinsic cell deformability, as expressed in eqn 3. To find the rate dP/dL, the suction pressure is gradually increased while the protrusion length is simultaneously recorded. When RBCs are completely suctioned into the micropipette, the threshold suction pressure (P_e) is used to determine cell deformability.[8]

$$\mu \propto {R_p}^2 \frac{dP}{dL} \tag{3}$$

Typically, measured values for red blood cell shear modulus (μ) range between 6–9 μN m^{-1} with an expected error as high as 20%.[74] Where shear modulus describes the elastic energy storage of the membrane under shear, the bending modulus (B_o) measures resistance to bending of the lipid bilayer.[75,76] Specifically, the bending modulus describes the amount of energy required to deform the membrane from its original curvature to a new curvature. In an early study of MPA, B_o was found to be 1.8×10^{-19} Nm,[76] which is consistent with values determined by subsequent studies using different methods.[29,77–79] MPA experiments requires personnel with considerable technical skills, as well as specialized equipment including a capillary puller, micromanipulator, microscopy system, and precision negative pressure source, such as an adjustable water reservoir. While MPA has been used to distinguish between RBCs treated with different concentrations of oxidizing agents,[80] this approach has very low throughput as only 20–40 cells are measured per test, due to the delicate and time-consuming cell manipulations. MPA has been used to measure the deformability of RBCs infected with *P. falciparum*, the parasite that causes malaria, which showed decreasing RBC deformability at more

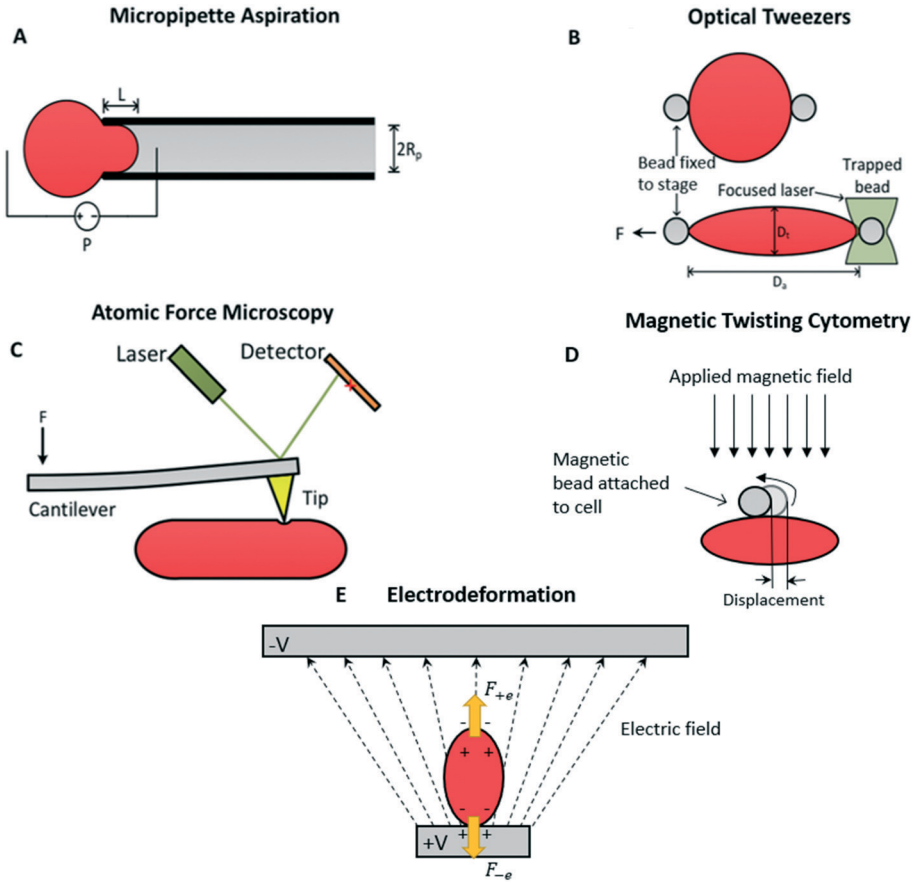

Fig. 2 Single cell techniques – micropipette aspiration, optical tweezers, atomic force microscopy, magnetic twisting cytometry, and electrodeformation. (A) Micropipette aspiration involves suctioning individual cells partially or completely into a micropipette to measure their deformability. (B) Optical tweezers involve attaching two microbeads to an RBC. A focused laser beam is then used to trap one of the beads while the microscope stage moves to elongate the RBC. (C) Atomic force microscopy involves using an AFM tip to deform the surface of the RBC. (D) Magnetic twisting cytometry measures RBC deformability by attaching a magnetic bead to the cell membrane and then applying a magnetic field. (E) Electrodeformation measures the RBC deformability by elongating a cell using an electric field.

advanced stages of infection.[8] MPA has also been used to study sickle cell disease[31] and diabetes,[17] where RBCs from these individuals were shown to have a higher shear modulus compared to healthy controls.

3.2 Optical tweezers

Optical tweezers measure RBC deformability by using lasers to pull on dielectric silica microbeads attached to the RBC membrane.[28–30,81] The beads are non-specifically attached to RBCs during incubation (Fig. 2B). The sample is deposited on a microscope slide and covered by a coverslip. The forces imposed on a microbead by a focused laser beam are first calibrated, typically by measuring the laser power needed to trap a bead in place while it is subjected to viscous forces resulting from Stokes flow.[28,30,81] At the point where the bead escapes the trap due to fluid flow, the optical trap force is the same as viscous drag force from the fluid, which can be determined by Stokes flow. After calibration, the force measurement is performed on an RBC with two microbeads fixed on the cell's membrane, with one attached to the microscope slide, and the other freely floating in the fluid. As the laser beam holds the free bead in place, the microscope stage movement elongates the RBC *via* the bead fixed to the stage. The applied force of the stage movement is increased until the trapped bead just escapes the optical trap. At this moment, the escape force (F), and the cell's transverse (D_t) and axial (D_a) diameters are recorded. From these parameters, the RBC deformation, defined as the elastic shear modulus or bending modulus of the membrane, can be determined using a model of the deformation process.[28,29] Example experimental-derived values for shear modulus and bending modulus using optical tweezers are μ = 2–13.3 μN m^{-1},[28,29,77] $B_o = 2 \times 10^{-19}$ Nm.[77] Accepted bending modulus values for red blood cells range between 1.7 to 7 × 10^{-19} Nm.[29] Deriving cell physical properties rely on mathematical models of cell biomechanics based on geometry, cytoplasmic viscosity, and viscoelasticity of the RBC membrane cortex structure.[79] These parameters can be difficult to quantify, resulting in a range of accepted values for the cell's physical properties. As such, values for these properties can vary between different techniques in part due to differing

idealized models of RBC mechanics, complicating their comparison.

Optical tweezers have been used to study RBCs infected with *P. falciparum* at different stages of infection.[6,82–84] This approach has also been used to study deformability of RBCs from patients with sickle-cell disease,[16,85] as well as RBCs stored in blood bags.[86–88] A major advantage of optical tweezers is the ability to select target cells identified by microscopy, enabling selection of rare cells, as well as integration with other measurement modalities, such as Raman spectroscopy.[89] The optical tweezers approach is also highly sensitive because of the ability to apply precise forces to the cell membrane. The disadvantage of optical tweezers is the need for specialized equipment and personnel, as well as its extreme low throughput (15–40 cells per test). Addressing these issues have been the focus of recent studies.[90]

3.3 Atomic force microscopy (AFM)

Atomic force microscopy measures the deformability of a section of the RBC membrane using a scanning probe integrated on a cantilever (Fig. 2C).[12,27] RBCs are first fixed to a microscope slide by chemically treating the glass surface. The tip of the AFM is brought into contact with a single RBC (Fig. 2C) and force is incrementally applied, generating a deformation on the RBC surface, and resulting in the deflection of the cantilever (Fig. 2C). The deflection of the cantilever is measured using a laser and a photodetector. The laser reflects off the cantilever and is directed to a different position on the detector depending on the angle of the cantilever. These deflections are converted into surface positions, giving the RBC indentation. The AFM apparatus can be calibrated using the constant compliance region of the force curve that is collected when the probe contacts the glass substrate prior to each experiment,[91,92] or by thermal calibration.[93] From the force *versus* indentation curve, the elastic modulus, or Young's modulus (E), of the surface is determined from a mechanical model of the RBC. According to AFM, the Young's modulus for healthy red blood cells can range from 1.10–7.22 kPa.[91–93]

AFM is an extremely sensitive instrument. A recent study showed that AFM could distinguish RBCs treated with 0.001% GTA from controls.[94] However, since AFM only measures the deformability of a portion of the RBC membrane instead of the overall cell, the result of this measurement is strongly influenced by the mechanical model of the RBC, as well as the accuracy of the parameters for this model. Additionally, AFM is very low throughput since only

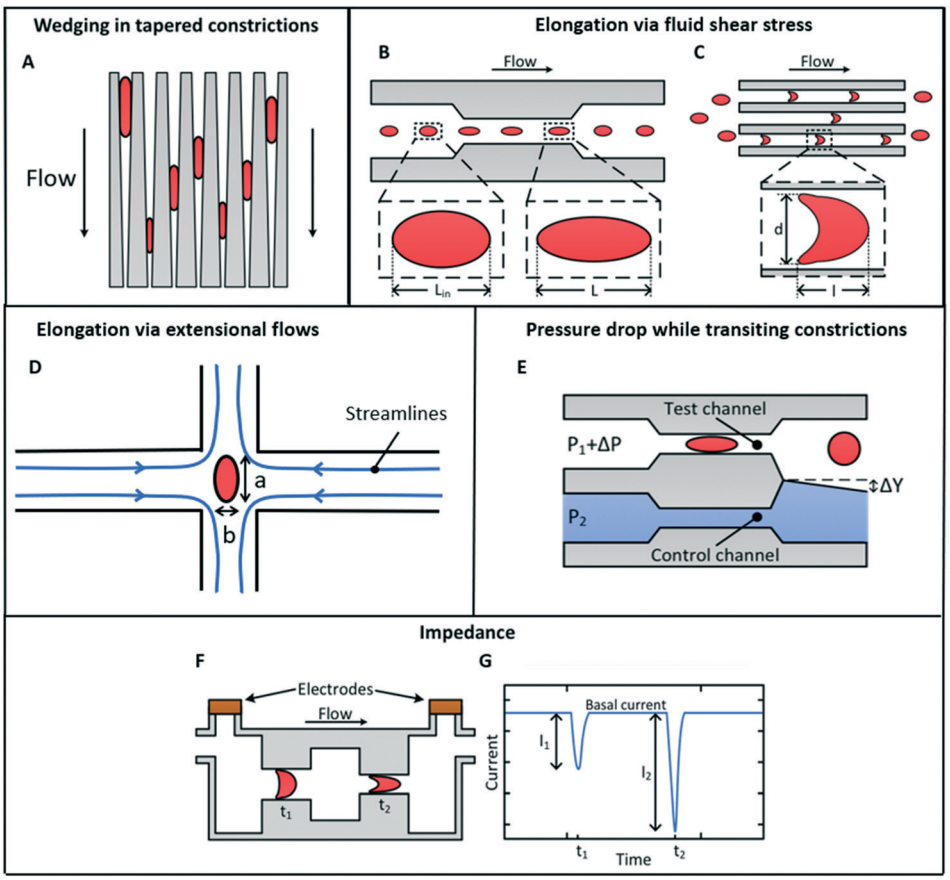

Fig. 3 Microfluidic techniques for measuring cell deformability (1/2). (A) Wedging in tapered constrictions. (B and C) Elongation *via* fluid shear stress. (D) Elongation *via* extensional flows. (E) Transit time through constrictions measured using pressure change. (F and G) Transit time through constriction measured using electrical impedance.

about 20 cells can be measured per test (or ~20 cells per hour, Fig. 6). One previous work has used AFM to study RBCs from patients with hemolytic anemias, including thalassemia, hereditary spherocytosis, glucose-6-phosphate-dehydrogenase deficiency, as well as patients with anisocytosis of various causes.[12] This study showed that pathological RBCs were more rigid than healthy RBCs. Similarly, AFM studies of RBCs from patients with diabetes mellitus were shown to have an increased average rigidity[95] as well as increased membrane roughness[96] compared to RBCs from healthy controls. In recent years, there are studies to automate AFM to improve throughput, as well as to combine AFM with other measurement modalities, such as infrared spectroscopy, to measure the topographical structures of biological samples.[27]

3.4 Magnetic twisting cytometry

Magnetic twisting cytometry involves applying both static and oscillating magnetic fields to ferromagnetic[97] or ferrimagnetic[78] microbeads attached to the cell membrane.[79] Based on the applied magnetic field, motion is induced on the microbeads translationally or rotationally (Fig. 2D), subsequently applying torque to the cell membrane that is captured optically.[78,79] The displacement of the bead in response to the applied torque can be used to find the dynamic modulus (or complex modulus) of the cell. The dynamic modulus describes the ratio of stress over strain for a viscoelastic material under periodic stress cycling conditions.[98,99] For a nonlinear system undergoing sinusoidal torque applications, the corresponding torque-displacement plot follows a sigmoidal hysteresis curve.[78] This response can be characterized by the storage (g') and loss moduli (g''), that sum complexly to produce the dynamic modulus (g^*).[78]

$$g^* = g' + ig''$$
$$g' = \frac{\Delta T}{\Delta d}\cos\phi \quad (4)$$
$$g'' = \frac{\Delta T}{\Delta d}\sin\phi$$

In eqn (4), ΔT and Δd are the torque and bead displacement amplitudes, and ϕ is the phase angle describing the corresponding lag between the applied torque and the subsequent bead displacement response.[100] If the frequency of the torque application is increased, the phase angle lag and loss modulus will increase, while the storage modulus is insensitive to frequency increases below 30 Hz.[78] The storage modulus can be considered a measure of the cell's stiffness while the loss modulus describes the membrane viscosity and is independent of the cell's elastic properties.[78,100] Using

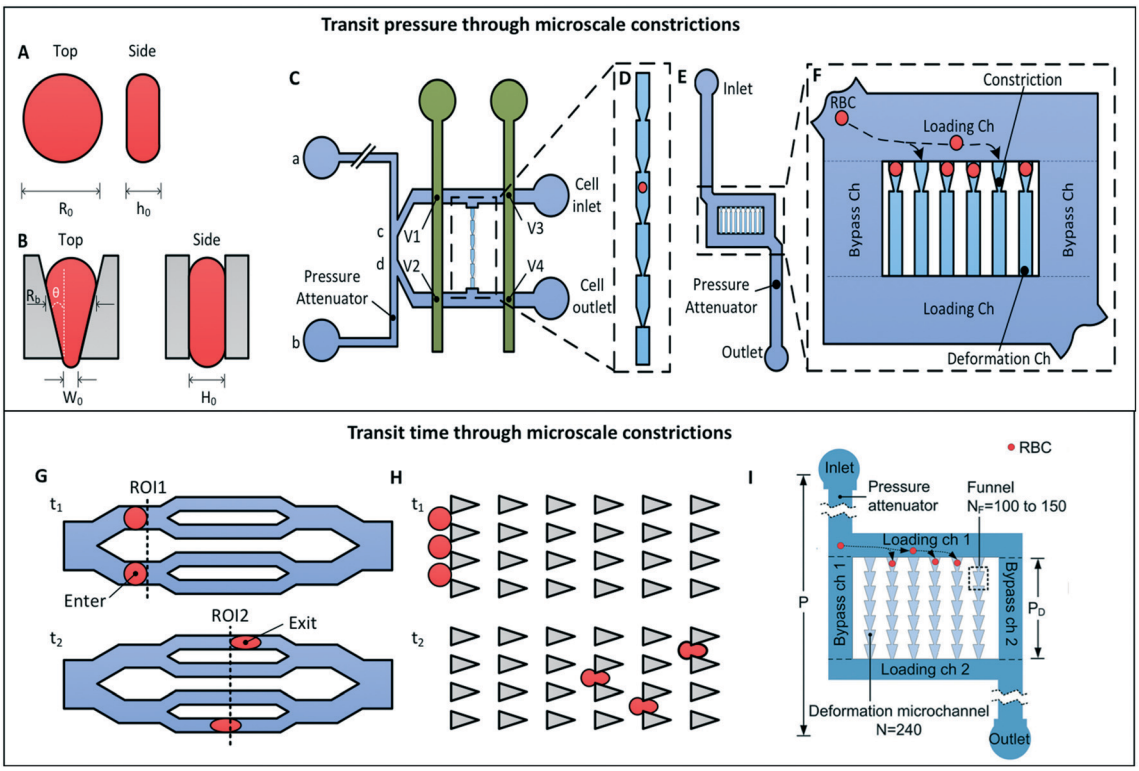

Fig. 4 Microfluidic techniques for measuring cell deformability (2/2). (A and B) Geometry of RBCs at rest and when deformed through micrometer scale constrictions. (C) The fluidic plunger device[5] with a (D) magnified view of the row of constrictions. (E) The multiplexed fluidic plunger device[116] with a (F) magnified view of the different constrictions and surrounding microchannels and the cell loading process. (G) Capillary network in the biophysical flow cytometer.[44] (H) Arrays of triangle-shaped pillars in the deformability-based flow cytometer.[43] (I) Rows of deformation microchannels in microfluidic cell-phoresis.[120]

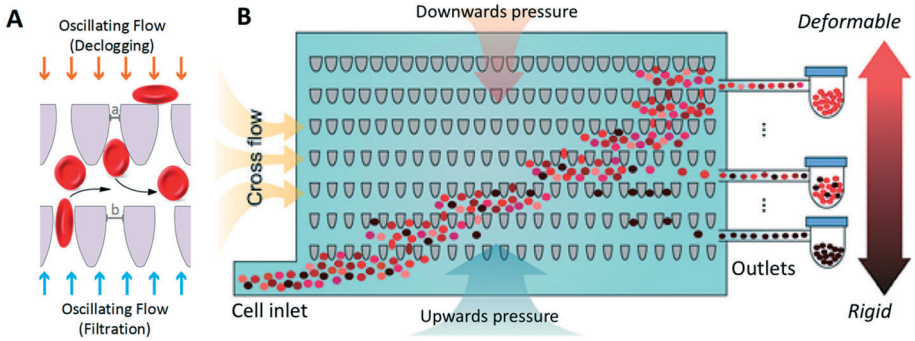

Fig. 5 Sort RBCs based on deformability. (A) Tapered funnel constrictions enable unidirectional transport of individual RBCs using oscillatory flow, which consists of upward filtration flow and downward de-clogging flow. (B) Deformability based cell sorting is performed using a matrix of funnel constrictions. The RBC sample is flowed into the lower left corner of the matrix and follows a diagonal trajectory resulting from vertical oscillatory flow and horizontal cross flow. RBCs travel diagonally through the matrix until reaching a limiting constriction size, which forces them to flow horizontally to a specific outlet. Deformable cells and rigid cells follow distinct paths because of different limiting constrictions.

this method, typical values for the storage modulus are $\sim 10^{-3}$ Pa nm^{-1} and the loss modulus linearly ranges from $\sim 7 \times 10^{-5}$ at 10^{-1} Hz to $\sim 7 \times 10^{-3}$ at 10^{2} Hz.[78] These parameters correspond to bending modulus values 2–8 $\times 10^{-19}$ Nm and shear modulus values 6–12 μN m^{-1}.[78,79] Further, magnetic twisting cytometry has been used to detect substantial increased stiffness of malaria-infected RBCs at the febrile temperature (41 °C).[79,101]

In optical magnetic twisting cytometry, only a small applied magnetic field is needed to deform the cells, allowing for easy multi-cell measurements. This method typically measures >100 cells per test.[102–105] Although magnetic twisting cytometry has been known to detect deformability differences between healthy cells and late-stage malaria-infected cells, it cannot differentiate healthy cells from early-stage ring cells, nor between trophozoite stage and schizont stage cells.[101]

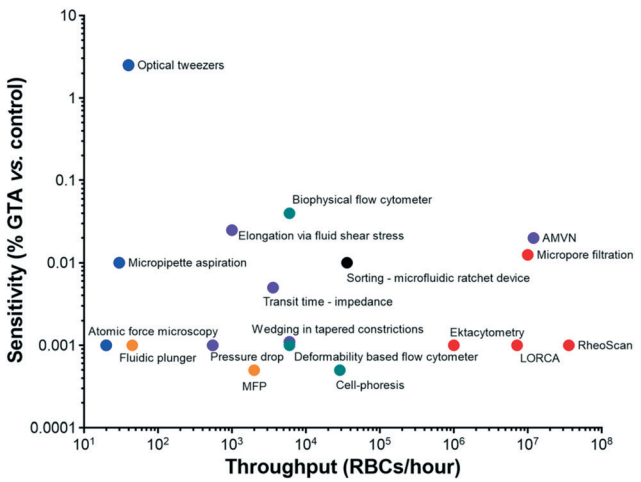

Fig. 6 Comparison of technologies for measuring RBC deformability. The sensitivity and throughput was determined by the ability of the device to measure the lowest concentration of GTA treated RBCs compared to control, while throughput was determined by the number of RBCs that could be measured per hour. Red – bulk flow, blue – single cell, purple, orange and green – microfluidics, black – sorting.

3.5 Electrodeformation

Electrodeformation methods measure the dynamic elastic behaviour of cells using dielectrophoretic force (Fig. 2E).[106–109] Optical images of the cells are captured using high-speed imaging during the deformation process, which enables determination of the elongation index (EI) and relaxation time once the applied force is removed.[107] These two parameters can then be used to determine the membrane shear modulus (~3.2–6.4 μN m^{-1}) and membrane shear viscosity (0.38–0.88 μN m^{-1} s^{-1}), which are comparable to results found with other techniques for healthy RBCs.[107,110] Interestingly, membrane shear modulus, shear viscosity, and relaxation time are dependent on the applied voltage and number of stress cycles. For example, after 1000 stress cycles, the RBC membrane shear modulus increases to 15 μN m^{-1}, which is indicative to fatigue in the RBC membrane. This increased RBC membrane rigidity is equivalent to a ring-stage RBC after infection by the *Plasmodium falciparum* malaria parasite.[110] Electrodeformation can be integrated into a microfluidic platform, allowing multiple microelectrodes to analyze many cells at higher throughput.[106,110–113] Microfluidic electrodeformation can achieve throughputs of 700 cells per mm^{2} per second, resulting in ~30 cells per test.[113]

4. Microfluidic techniques

Traditional single cell deformability measurement techniques require complex experiments that typically can only be performed by skilled personnel using specialized equipment.[114] These methods are also very low throughput, which limit their ability to profile a heterogeneous RBC population, such as in cases where diseased cells comprise a fraction of the entire population. The complexity of these techniques also makes them unsuitable for routine clinical analysis or point-of-care analysis. Microfluidics technologies have the potential to address these challenges by providing

simpler measurements that could be performed with greater throughput.[115] Recently, there have been significant new developments in microfluidic mechanisms for measuring RBC deformability including those based on wedging in tapered constrictions,[33,34] elongation *via* applied fluid flows,[35–40] transit time through constrictions,[41,42] transit pressure through microscale constrictions,[5,116–119] deformation through a series of constrictions,[43,44,120] and sorting of RBCs by their deformability.[45,46]

4.1 Wedging in tapered constrictions

Wedging in tapered constrictions involves microfluidic devices containing a row of tapered constrictions (with dimensions <5 μm, Fig. 3A), such as the human erythrocyte microchannel analyzer (HEMA) device.[33,34] Individual RBCs are squeezed into the constrictions due to a flow *via* applied pressure. Since the cells have variations in volumes, surface areas, and membrane tensions, they reach different equilibrium positions in the tapered constrictions. Their position and the geometry of the constrictions are used to calculate their area-to-volume ratio, which defines the deformation of each RBC. In addition, the membrane cortical tension of each cell can be estimated using the law of Laplace,[33]

$$\Delta P = 2T_c\left(\frac{1}{R_A} - \frac{1}{R_B}\right) \quad (5)$$

where ΔP is the pressure drop across the microchannel, T is the membrane tension, R_A is the leading cell radius, and R_B is the trailing cell radius.

The device contains a large number of tapered constrictions, allowing a high throughput analysis at the rate of 100 cells per min.[33] These constrictions are in parallel with several wide constrictions that allows the free passage of RBCs around them. Since the hydrodynamic resistance of the tapered constrictions represents only 0.7% of the total array resistance, partial blockage of occupied tapered constrictions doesn't significantly affect the flow.[33] Therefore, clogging of some tapered constrictions does not affect the suction pressure that the other RBCs experience at other constriction sites. This device is easy to operate. The optical measurement of cell position are accurate to within 0.2 μm, comparable with the tolerances of the photolithographic process used to fabricate the microfluidic channels.[34] However, this method primarily investigates the area-to-volume ratio, but it can be difficult to determine the overall cell deformability. For example, in RBCs infected with *P. falciparum*, a deformability difference was observed between uninfected and late stage schizont-infected RBCs, but was not sensitive enough to distinguish them from intermediate stage trophozoite-infected RBCs.[34]

4.2 Elongation *via* fluid flow

4.2.1 Elongation *via* fluid shear stress. Elongation *via* fluid shear stress applies shear stress to individual RBCs in narrow microchannels controlled using pressure-driven flow (Fig. 3B and C). The resulting elongation of RBCs is measured using a high-speed camera.[35,36] In one realization of this approach, known as the artificial microvascular network (AMVN), the dimensions of the microchannels range from 5 μm to 70 μm to simulate different capillary sizes. RBCs are deformed differently based on the dimensions of the microchannel. When the dimension of the constriction is similar to the diameter of a single RBC, the RBCs is stretched by fluid shear stress.[35] In this case, RBC deformability is defined as the ratio of the deformed longitudinal length (L) and the initial length (L_{in}) of the RBCs (Fig. 3B). In the larger capillaries of the AMVN, RBCs deform in a parachute-like shape as they undergo shear-induced deformations as well as deformations caused by collisions with other RBCs in the bulk flow.[36] In this case, the deformability index (DI) is defined as the ratio between the length (l) and the diameter (d) of the deformed RBCs (Fig. 3C), as indicated in eqn (6).

$$\mathrm{DI} = \frac{l}{d} \quad (6)$$

The DI of each RBC is correlated to its own velocity to obtain the overall flow rate of the RBC sample under study, which can then be compared between treated samples. The shape changes of the deformed RBCs rely on optical measurements with sub-micrometer accuracy using high-speed cameras and microscopy.[42] There are significant data processing requirements since images are captured at one frame per second for 10 minutes.[42] However, the device is easy to operate and mimics flow in the microvasculature. The AMVN was validated using 0.05% and 0.025% GTA-treated RBCs from control and has been used to study RBC deformability in diabetes patients.[35,36]

A variation of this method involves the use inertial focusing to align and deform RBCs in a viscoelastic fluid.[121] In viscoelastic Poiseuille flow, a lateral lift force allows cells migrate to a specific position in a microchannel, where they are subsequently deformed due to non-normal stress distributions created by fluid interaction with the wall. The position, angle, and DI of each cell is then determined using digital in-line holographic microscopy, which can be assessed at a throughput of 2500 cell per s.[121]

4.2.2 Elongation *via* extensional flows. Another approach for deforming cells using fluid shear stress is *via* extensional flows. This technique uses flow from two opposing microchannels to deform RBCs in a perpendicular junction (~50 μm across) using viscous fluid stress[37–40] (Fig. 3D). This method can generate applied stresses an order of magnitude greater than other methods, including atomic force microscopy and micropipette aspiration.[39,122] The resulting deformed cell shape is assessed using a high-speed camera attached to an inverted microscope. RBC deformability is quantified using the ratio between the major axis (a) and minor axis (b) length of each cell (see Fig. 3D).[38–40]

Inertial focusing has been used to align flowing cells in an ordered manner.[123–125] Inertial focusing has been coupled

with elongation *via* extension flows to deliver suspended cells uniformly to the perpendicular junction, achieving deformation assessments of nucleated cells at throughputs of ~2000 cells per second.[39] However, to our knowledge, inertial focusing of RBCs has not been integrated with elongation *via* cross-slot extensional flows. One obstacle is that RBCs have significantly less mass and greater deformability than nucleated cells, which makes them more difficult to manipulate using inertial forces.

4.3 Transit time through constrictions

4.3.1 Measured using pressure drop. This approach measures the time required to deform individual RBCs through a ~5 μm constriction located in the test microchannel using the pressure drop change measured in a parallel control microchannel (Fig. 3E).[41] The pressure applied across both the test and control channel is fixed by the structure of the microchannel and the flow rate is provided by infusion using a syringe pump. The control channel is infused with a dyed liquid in order to visualize the boundary of the fluid flow between the test and control channels. When an RBC flows into the test channel, the boundary of the fluid flow is deflected as displacement (ΔY) by the increased pressure (ΔP) across the test channel. To associate the interface deflection with a corresponding pressure drop change, the device is first calibrated with both channels remaining empty, where the deflection of the interface is recorded for different applied pressure of the test channel inlet (P_1) while the pressure of the control channel inlet remains unchanged (P_2). For a given P_2, a linear relationship exists between these pressure increments and associated deflections. Next, the deformability, here defined as the pressure drop, can be calculated from the slope of the obtained curve (A), as expressed in eqn (7).

$$\Delta P = \frac{\Delta Y}{A} \tag{7}$$

Similar to elongation *via* fluid shear stress, this method is simple to use, mimics deformation in the microvasculature, but also requires the use of a high-speed camera to perform interface deflection measurements during each RBC transit. Pressure drop is sensitive to the number of RBCs simultaneously transiting through the test channel and to cell clogging at the entrance. Consequently, the cell density must be controlled to obtain single cell transits and the throughput is possibly limited. While this device could only distinguish RBCs treated with 0.001% GTA, it has also incorporated more sensitive measurements of other indicators, such as ATP release and macroscopic viscosity at physiological shear rates.[126] With these additional characteristics, hemoglobinopathies, diabetes and blood storage are potential applications of this technology.

4.3.2 Measured using electrical impedance. RBC transit time through micrometer scale constrictions can also be measured using electrodes located on either side of constriction-containing microchannels.[42] One realization of this approach used a microchannel with two constrictions: one similar to the diameter of RBCs and one smaller than the diameter of RBCs (Fig. 3F). An electrical current is applied across this microchannel. When no cells are transiting through the constrictions, the electrical current measured *via* the electrodes is constant (basal current, Fig. 3G). When an RBC is present in one of the constrictions, fluid flow is partially obstructed, which causes a reduction in the measured electrical current due to the increased electrical resistance across the constriction. This signal change can be visualized as valleys in the current *versus* time graph (I_1 and I_2, Fig. 3G). The two different sized constrictions generate different electrical signal changes. In order to obtain both valleys, the two constrictions are located apart in the main large microchannel. For the first constriction, the RBC deformation is negligible. Consequently, the electrical signal decrease, or small valley (I_1), is proportional to the cell size only. In the case of the second constriction, each individual RBC is deformed in a parachute-like shape. Therefore, the signal, or large valley (I_2), decreases in relation to the combination of cell size and deformability. RBC deformability, defined as mechanical opacity, is then obtained from the ratio of the large and small valley currents, as expressed in eqn (8).

$$\text{Mechanical Opacity} = I_2/I_1 \tag{8}$$

The major advantage of this approach is the decoupling of the volume and size of the RBC from its deformability. Additionally, measurements performed using this approach is very fast since 1000 cells can be measured at a speed of 60 cells per min. One potential issue is that each RBC must be measured by two constrictions set apart from each other, and if the throughput is too high that multiple cells are present between the electrodes, it could potentially confound the measurement. The measured current is also sensitive to constriction blockage due to cell clogging. These devices have been shown to be able to distinguish GTA (0.005%) and heat-treated RBCs from control.[42] Recent studies have improved the sensitivity and throughput of this approach to determine the deformability alteration that occurs in hereditary spherocytosis and sickle cell disease.[127–129]

4.4 Transit pressure through constrictions

Measuring the pressure required to deform single RBCs through a microscale constriction involves a mechanism known as the fluidic plunger (Fig. 4).[1,5,116,130,131] This approach initially infuses individual RBCs into a microchannel containing a constriction of 1–3 μm in width. When the RBC is free to move, the applied pressure is distributed across the microchannel. However, when the RBC reaches a constriction, it blocks the constriction and the pressure applied to the microchannel is applied remotely across the RBC (Fig. 4A and B). The threshold transit

pressure of single RBCs can be measured by varying this applied pressure.

The initial version of the fluidic plunger, developed by Guo, *et al.*,[1,5,130] contains a row of constrictions varying in size (from large to small, Fig. 4D), which enables precise RBC deformability measurements. An intrinsic measure of RBC deformability can be obtained from the cortical tension (T_c), which is derived using the liquid drop model of RBCs,[74] which can be calculated from the threshold pressure (P_D) required to transit the cell and the geometry of the constriction used, as described in eqn (9). Since the value of P_D ranges between 1–25 Pa for RBCs, the device contains a pressure attenuator network that reduces an externally applied pressure to a smaller pressure based on the ratio of the hydrodynamic resistance (the pressure applied across the microchannel between (a) and (b) is divided by a factor of 100 over the microchannel segment between (c) and (d), Fig. 4C).

$$T_c = \frac{P_D}{\frac{2}{W_0} - \frac{1}{R_b}} \quad (9)$$

The process to perform measurements using the fluidic plunger mechanism involves using microfluidic valves V1–V4 to isolate and measure individual cells.[132] This process is cumbersome and therefore only 25–40 cells could be measured per test. Cell clogging is also a potential issue since the device contains only a single row of constrictions. This process is very sensitive and has been shown to distinguish RBCs treated with 0.001% GTA and control.[131] The fluidic plunger device has been used to distinguish different stages of malaria infected RBCs,[5] as well as to study potential new antimalaria drugs.[133]

To increase the throughput of the fluidic plunger, Myrand-Lapierre, *et al.* developed the multiplexed fluidic plunger (MFP) device, which comprises multiple constrictions in a parallel set of microchannels, surrounded by a much larger rectangular bypass microchannel (Fig. 4E and F).[116] The MFP device simplifies sample loading because it consists of a single inlet and outlet, and all RBCs transiting the micro-constrictions experience a constant pressure that is independent of the number of occupied constrictions.[116] Under these measurement conditions, the MFP device is able to distinguish 0.0005% GTA-treated RBCs compared to control. Measurements can be obtained for 2000 cells per test, where measurement throughput is limited by the number of constrictions that can be simultaneously imaged within the microscope field of view. The device can detect *P. falciparum* infection[116] and has been used to determine the efficacy of multiple antimalarial drugs on infected RBCs,[117] as well as changes in RBC deformability in response to hemolytic stress.[119] The MFP was used to measure changes in deformability during cold storage in order to identify the proportion of RBCs that may be rapidly cleared by the spleen in a transfusion recipient.[118]

4.5 Deformation through a series of constrictions

Another approach for measuring RBC deformability is to repeatedly deform RBCs through a series of constrictions smaller than their diameter.[43,44] RBC deformability could then be determined from the time required to traverse through a set number of constrictions or the number of constrictions traversed in a given time period. Multiple designs have been developed using this approach: a capillary network called the biophysical flow cytometer (Fig. 4G);[44] arrays of periodically spaced triangle-shaped pillars called deformability flow cytometry (Fig. 4H);[43] and rows of deformation microchannels in microfluidic cell-phoresis (Fig. 4I).[120]

In the biophysical flow cytometer, the capillary network consists of microchannels that bifurcate into smaller microchannels.[44] Cell deformability is characterized by the time required for the RBCs to travel between two points in the network, called regions of interest (ROIs), which are located before and after the smallest microchannels (Fig. 4G). Transit time measurements depend on the relaxation of the RBC membrane in response to bending.[43] Since the mechanical time constant for bending RBC membranes is $\ll$1 second,[134] the sensitivity and throughput of this technology is expected to be high. Indeed, this method is sensitive and can distinguish between RBCs treated with 0.04% GTA and controls and can measure 50–100 cells per min.

In the deformability-based flow cytometer, each RBC travels through a row of constrictions (Fig. 4H).[43] The deformability is defined by the velocity of the cells. The sensitivity and throughput of this method was shown to be high, with the detection of a GTA concentration of 0.0005% compared to control. The measurement throughput is 100 cells per min with the ability to measure up to 10 000 cells per test.

In microfluidic cell-phoresis,[120] single RBCs are loaded into the entrance to microscale constrictions using a pressure that is insufficient for them to transit. Once the majority of the deformation microchannels are filled with RBCs, a deformation pressure is then applied to push the cells through the constrictions. The deformability of each cell can be determined from their final position, similar to DNA bands after gel-electrophoresis. The RBC deformability results obtained can reliably distinguish between control and 0.0005% GTA fixation, with the ability to measure 240 cells per test that can be multiplexed (prototype multiplexes 8 devices). This device was also used to detect malaria infection, as well as to study how infected RBCs are affected by existing and potential antimalarial drugs, including artesunate,[135] (+)-SJ733, and NITD-246.[120]

4.6 Sort red blood cells based on deformability

The microfluidic ratchet device (Fig. 5) sorts RBCs through a 2D array of micrometer scale tapered constrictions that are gradually decreased along the flow path, forcing RBCs to

deform as they transit through progressively smaller openings (1.50–7.5 μm). Due to the geometric asymmetry of the taper, the force required to deform cells through the constriction along the direction of taper is less than against the direction of taper.[136] Oscillatory vertical flow and horizontal cross flow forces cells to move diagonally through the sorting array until they can no longer transit a specific sized constriction and are routed towards 12 distinct outlets. Importantly, this oscillatory flow also minimizes the contact between cells and the filter microstructure to prevent clogging and fouling and to ensure that a consistent filtration force is applied to each cell.[137] After deformability-based cell sorting, the distribution of RBCs in outlets 1–12 can be shown as a histogram. In order to effectively compare differences between samples, the result is plotted as a cumulative distribution, which provides a "rigidity score" as the fractional outlet number where the cumulative distribution function crosses 50%. This fractional value for the rigidity score can be obtained by linear interpolation between data points in the cumulative distribution function.

This device is capable of sorting ~600 RBCs per minute and is shown to separate GTA-fixed RBCs into distinct outlets corresponding to the amount of GTA used down to 0.01% GTA.[45,46] Despite this method having lower sensitivity compared to some other methods, it benefits from being highly repeatable.[138,139] This allows the device to be more easily used to characterize the deformability of multiple individuals quickly and with high consistency. Furthermore, this device has been shown to enrich for ring stage plasmodium infected RBCs by >100×, to improve diagnostic sensitivity of rapid tests.[45] It has also been used to study deformability changes of RBCs during cold storage, but perhaps the most important finding was that there are differences in deformability profiles of healthy blood donors and these profiles are conserved during storage.[46]

5. Imaging and machine learning techniques

Imaging and computation methods are essential aspects of many of the bulk flow, single cell, and microfluidic techniques described previously. However, several recent studies are beginning to demonstrate the potential to assess RBC biophysical properties directly using imaging and computation.

5.1 Quantitative phase imaging

Quantitative phase imaging (QPI) captures the amplitude and phase delay of laser light reflected on a sample by interfering this light with the incident laser light.[79,140] QPI have been used to capture the thermodynamic membrane fluctuations of RBCs,[141–144] which has been shown to be strongly correlated with RBC deformability.[145] Early QPI techniques were limited by phase noise due to mechanical vibrations and air fluctuations affecting the interferometric system, preventing the acquisition of highly sensitive quantitative phase images.[146] There issues were alleviated by the development of the diffraction phase microscopy, which uses common-path laser interferometry to cancel most noise mechanisms and employs a single-shot acquisition, where camera acquisition speed is the only limitation on acquisition throughput.[79,141] This approach provides highly stable QPI, characterized by capturing nanoscale motions of cell membranes,[147] and can be used to determine RBC shear modulus, bending modulus, area expansion modulus, and cytoplasmic viscosity.[144]

5.2 Emerging machine learning techniques

Machine learning using convolutional neural networks excels at image classification based on training using large quantities of labeled image data.[148,149] Deep learning has been used to determine material parameters of the constitutive RBC model, as well as the corresponding stress–strain relationship.[148] Recently, advances in imaging flow cytometry have enabled high throughput assessments of RBC morphological changes associated with the storage lesion.[150] RBC morphological changes that occur during storage are also related to decreased deformability.[46] To help assess the large numbers of imaging data and improve the data analysis pipeline, deep learning techniques have been applied to imaging flow cytometry data. Deep learning assessment of label-free imaging flow cytometry data determined RBC morphological changes associated with the storage lesion with similar agreement compared to experts.[151] Since the morphological changes due to the storage lesion are associated with decreased deformability, deep learning techniques were extended to assess RBC deformability directly.[152] In this study, RBCs were sorted based on deformability through a microfluidic ratchet sorting device, and subsequently sorted cells were imaged using brightfield microscopy at 40× magnification. These images were used to train and test the deep neural network, achieving deep learning-derived rigidity scores within 10.4 ± 6.8% of the values derived from cell sorting using the microfluidic ratchet device.[152] Additional work will be required to assess the generalizability of this approach, but there are indications of the research potential of this area. For example, there is emerging indications that machine learning-enabled technologies can aid the assessment of RBC quality for transfusion.[153]

6. Comparison of technologies

We compared technologies for measuring RBC deformability in Table 1 and Fig. 6. The key performance parameters for each technology are throughput and sensitivity. Throughput is defined by the number of RBCs measured per test or per hour, with low, medium, and high throughput being defined as <100 cells per test or <500 cells per hour, 100–1000 cells per test or 500–3000 cells per hour, and ≥1000 cells per test

Table 1 Comparison of different technologies for measuring RBC deformability

	Technique	Deformability	Throughput Low: <100 cells per test, <500 cells per hour Medium: 100–1000 cells per test, 500–3000 cells per hour High: ≥1000 cells per test, ≥3000 cells per hour	Sensitivity (% GTA *vs.* control) Low: >0.050% Medium: 0.050–0.0010% High: <0.0010%	Measure single RBCs (Y/N)	Robust to clogging (Y/N)	Key challenges
2.1	Ektacytometry LORCA/LoRRca RheoSCAN	Elongation index (EI)[21–23]	High ~10^6 cells per hour	Medium 0.0010%	N	Y	Requires sample washing and resuspension in different mediums
2.2	Micropore filtration	Deformability index (DI)[24,25]	High	Medium	N	N	Requires processing to remove leukocytes and other cells to prevent clogging
			~10^7 cells per hour	0.0125%			Does not provide a quantitative measurement
3.1	MPA	Shear modulus[31,8,32]	Low	Medium	N	Y	High measurement error rate (~20%) between samples
			~30 cells per test	0.0100%			Selection bias
3.2	Optical tweezers	Shear modulus[28–30]	Low	Low	N	Y	Sample manipulation at the single cell level which requires skilled personnel
			~40 cells per test	2.5000%			Selection bias
3.3	AFM	Young's modulus[12,27]	Low	Medium	N	Y	Only measures a portion of the RBC membrane
			~20 cells per test	0.0010%			Selection bias
3.4	Magnetic twisting cytometry	Dynamic modulus[78]	Medium ~100 cells per test	—	N	Y	Measures a select area of the RBC membrane
3.5	Electro-deformation	Elongation index (EI)[107]	Low ~30 cells per test	—	N	Y	Derived biophysical properties are dependent on the magnitude of the applied voltage
4.1	Wedging in tapered constrictions	Area-to-volume ratio[33,156,34]	High	Medium	Y	Y	Optical measurements are accurate only with expensive camera equipment
			~6000 cells per hour	0.0011%			Investigates the area-to-volume ratio and can be difficult to determine the overall cell deformability
4.2.	Elongation *via* fluid shear stress	Deformation[35]	Medium ~100 cells per test	Low	N	N	High speed camera required
		Deformation index (DI)[36]	High ~1000 cells per test	0.0250%	N	Y	Different sized microchannels makes measurement difficult – significant data processing required
	Elongation *via* extensional flows	Ellipse major–minor axis ratio[38–40]	High	—	N	Y	High speed camera required to capture changes in RBC shape
		Deformation index (DI)[37]		—	N		Numerical methods outcomes need to be validated with *in vitro* experiments

Table 1 *(continued)*

	Technique	Deformability	Throughput Low: <100 cells per test, <500 cells per hour Medium: 100–1000 cells per test, 500–3000 cells per hour High: ≥1000 cells per test, ≥3000 cells per hour	Sensitivity (% GTA *vs.* control) Low: >0.050% Medium: 0.050–0.0010% High: <0.0010%	Measure single RBCs (Y/N)	Robust to clogging (Y/N)	Key challenges
4.3	Pressure drop	Pressure[41]	Medium ~500 cells per hour	Medium 0.0010%	N	N	Requires significant sample dilution High speed camera required
	Electrical impedance	Mechanical Opacity[42]	High ~3600 cells per hour	Medium 0.0050%	N	N	Requires significant sample dilution to prevent measurement error
4.4	Transit pressure	Cortical tension[1,5,130,131]	Low 40 cells per test	Medium 0.0010%	N	N	Measurement is time consuming and requires skilled personnel
		Pressure[116]	High ~2000 cells per test	High 0.0005%	Y	Y	Measurement is limited by microscope field of view
4.5	Transit time	Time[44]	High ~6000 cells per hour	Medium 0.0010%	Y	N	Requires sample processing to remove leukocytes and other cells to prevent clogging
		Velocity[43]	High ~3600 cells per hour	High 0.0005%	Y	N	Devices need to be calibrated
4.6	Cell sorting	Rigidity score[46]	High ~36 000 cells per hour	Medium 0.0100%	Y	Y	Requires specialized pressure board and skilled personnel for operation Cumulative distribution and interpolation of deformability profile needs to be established for each sample
5.1	Quantitative phase imaging	Shear modulus[144]	High	—	Y	n/a	Limited to measuring line integral of the refractive index and optical path length, thus details are lost in the *z*-direction[141]
5.2	Machine (*e.g.*, deep) learning	Morphological characteristics[151,152]	High	—	Y	n/a	Emerging technology – generalizability not confirmed

or ≥3000 cells per hour. Sensitivity is assessed based on the ability to distinguish RBCs treated using mild GTA fixation from matched control with low, medium, and high sensitivity being defined as >0.05%, 0.05–0.01%, and <0.01%. As discussed earlier, GTA is a common fixative that induces cross-linking and stabilization of proteins in the RBC membrane and thus artificially reduces their deformability in a concentration dependent manner.[154,155] Additionally, we assessed the ability of each method to measure single cells, robustness against clogging by rigid RBCs or RBC aggregates, as well as note key challenges associated with each method.

From the comparison in Table 1, we can see bulk flow technologies excel at evaluating vast numbers of cells, but these techniques are unable to assess RBC sub-populations. The traditional single-cell technologies have similar sensitivities to the bulk flow techniques (with optical tweezers being an exception) but suffer from greatly reduced throughputs. Microfluidic techniques blend the benefits from traditional bulk and single-cell techniques – providing

higher throughput with equal or greater sensitivity, as well as single cell measurements. For example, microfluidics for measuring transit pressure or time, shows both greater sensitivity and greater throughput over any of the conventional methods. Furthermore, the ability to distinguish small changes in subpopulations of pathological cells within the bulk population has broader applications in disease diagnosis and treatment efficacy, as discussed in the next section. Finally, advances in imaging and machine learning could enable measurements without specialized equipment.

7. Applications

Since cell deformability is an indicator of RBC function, this parameter could be used as a potential biomarker for the quality of RBC used in blood transfusions, or for RBC dysfunction resulting from certain diseases. Here, we discuss some of the biological processes that degrade RBC deformability as well as the technologies have been applied to several different areas of research and development to assess blood quality, disease status, and drug efficacy.

7.1 Blood storage and transfusion medicine

RBC transfusions are used to meet the complex needs of recipients, which arise from blood loss resulting from trauma, surgery, and child birth,[157,158] as well as the management of chronic disorders, such as severe kidney disease,[159] bleeding disorders,[160] hemoglobinopathies (*e.g.* sickle cell disease and thalassemia),[161] and recovery from certain chemotherapies.[162] While RBC transfusions are relatively safe for acute transfusion recipients, chronic transfusions pose significant risks and adverse-effects for recipients, including iron-overload, transfusion related acute lung injury (TRALI), hypervolemia, and increased risk of infections.[163–165] Therefore, a long-standing challenge in transfusion medicine has been to reduce the frequency of chronic transfusions by increasing the circulation time of transfused RBCs in recipients.

Not all donated RBC units will circulate for the same amount of time in transfusion recipients. In fact, there is significant variability in the circulatory half-life and rates of degradation of RBCs across different donors,[118,166] with some RBC units able to circulate for long periods of time in recipients to maintain hemostasis, while other units are rapidly cleared, leading to the need for repeat transfusions.[167,168] These variations can be the result of many different factors, including genetics, age, sex, diet, metabolism, lifestyle factors, and presence of subclinical illness.[169–172] Therefore, the assessment of donated RBCs requires repeatable measurements with sufficient sensitivity to assess this variability between donors.

The deformability of RBCs has long been considered as a potential biomarker of RBC circulation time. Cold storage of RBCs for use in blood transfusion can significantly decrease RBC deformability. This degradation is part of what is known as the RBC *storage lesion*[173,167] that develops due to structural (lipid peroxidation, band 3, membrane asymmetry), metabolic (slowed metabolism due to ATP and 2,3-diphosphoglycerate depletion), and morphologic (discoid, echinocyte, and spherocyte)[156] transformations. The loss of RBC deformability typically commences after 2 weeks of cold storage and accelerating thereafter.[25,60,86,118,174] RBCs with reduced deformability has also been shown to result in diminished circulation time *in vivo.*[1] More recently, several studies have identified donors with RBCs that have the potential of maintaining their deformability longer than other donors.[46,118] In another study, a donor with low RBC transfusion viability was found to have normal routine hematological parameters, but the deformability of the RBCs decreased at a faster rate *in vitro* compared to typical donors.[60,118] These types of studies are likely to ultimately show that donor variability in RBC deformability loss may strongly impact post-transfusion outcomes.[175–177]

Future studies should focus on the differences between healthy donors as a means to select donors that could provide long-circulating RBCs for sensitive recipients. Preferentially providing chronic transfusion recipients with long-circulating RBC units would dramatically improve outcomes for these patients, as well as increase the overall blood supply. Another potential challenge in analyzing the loss of RBC deformability during cold storage is that this loss may be restricted to a small fraction of the overall RBC population. Therefore, while individual cells may experience loss of deformability due to the storage lesion, this degradation may not be apparent from bulk measurement of the blood population. Consequently, transiting away from population-based measurements towards high-throughput single cell measurements is critical to addressing the current challenges of RBC product quality.

An important related issue for future studies is the sampling of RBCs from blood bags, which is difficult to do without compromising the product. A potential alternative is to sample the blood bag segment tubing attached to the blood bag unit. Recently, it was shown that RBCs sampled from these blood unit segments accurately represent the biophysical properties of RBCs in blood bags.[139] This result could enable future studies of donor RBCs linked to outcomes in transfusion recipients.

7.2 Malaria

Malaria, caused by *P. falciparum*, remains one of the greatest problems in human health with an estimated ~229 million infections per year resulting in over 400 000 deaths per year.[178] Although the clinical manifestations of severe malaria occur at different anatomical sites, many of these manifestations result from invasion and infection of RBCs by the parasite.[179] During this intraerythrocytic stage, the parasite acquires heme from host hemoglobin.[180] Within the infected RBC (iRBC), the parasite undergoes asexual multiplication and matures to form schizonts. The schizonts

ultimately rupture to release merozoites, which subsequently infect neighboring RBCs.[5,6] As the infection spreads among RBCs, parasite gene expression promotes the sequestration of those RBC within vascular beds.[181] Lysis of RBCs following erythrocytic schizont stage as well as splenic clearance of iRBCs contributes to anemia while obstruction reduces oxygen delivery to tissues and contribute to cerebral complications.[182]

Alteration in RBC deformability is central to malaria pathology since changes in RBC deformability impact both the severity of infection and the efficacy of antimalarial drugs. Infection of RBCs contributes to reduced deformability of iRBCs[5–8] due to heme-mediated oxidation resulting from the metabolism of hemoglobin, deposition of parasite proteins onto the iRBC membrane, as well as the presence of the parasite bodies and digestive vacuole.[7,8,183–185] Furthermore, the free heme that is released when schizonts rupture[119,186,187] results in oxidative membrane damage to uninfected cells.[6,23] The rigidification of iRBC is unfavorable to the persistence of the parasite, as rigid iRBCs are rapidly removed from circulation through splenic clearance.[2] Consequently, the parasite slows the loss of deformability by biocrystallization of heme into hemozoin. Conversely, antimalarial drugs such as chloroquine potentiate heme toxicity and iRBC rigidification by disrupting hemozoin formation.[188] These observations collectively suggest that that RBC rigidification contributes significantly to clinical outcomes and antimalarial drug efficacy.[23,189–191]

Therefore, technologies for measuring RBC deformability can be used to detect malaria infected RBCs, as well as to evaluate disease severity and drug efficacy. A key challenge in obtaining this physical biomarker is that the infected RBCs typically comprise of <2% of the overall RBC population, which means that the average RBC deformability measured using existing instruments (*e.g.* ektacytometry) is insufficient to detect the subpopulation of infected RBCs. These technologies should be able to measure single RBCs at high throughput to be able to detect the small RBC deformability changes of ring-stage iRBCs,[5,6] as well as the small rigid subpopulations of iRBCs (as low as 0.2%). One study, using the Multiplexed Fluidic Plunger device demonstrated the potential of using RBC deformability as a means to detect infection in samples with a parasitemia as low as 1.8% with 82% specificity,[116] while Microfluidic Cell-phoresis could detect parasitemia as low as 0.2%.[120] Cell sorting using the microfluidic ratchet device successfully enriched for ring stage plasmodium iRBCs by >100×, to improve diagnostic sensitivity of rapid tests.[45]

Furthermore, the effect of antimalarial drug treatment on the deformability of *P. falciparum* iRBCs *in vitro*, have been under investigation. Rigidification of iRBCs has been reported a common outcome of *in vitro* antimalarial treatment that may enhance splenic clearance *in vivo.*[192] Ektacytometry has been unable to ascertain changes in iRBC deformability induced by treatment with artesunate.[193] However, microfluidic devices based on the transit time though microscale detected deformability changes of ring-stage iRBCs treated with artesunate,[120,135] using devices that were medium to high throughput and were robust to clogging. These devices performed single cell deformability measurement of iRBCs, enabling the measurement of iRBC sub-populations. These studies revealed that changes in iRBC deformability could serve as potential biomarkers for anti-malaria drug discovery.[116,117,133,194]

7.3 Hemoglobinopathies

Hemoglobinopathies are hereditary conditions, such as thalassemia and sickle-cell disease, that result in the production of abnormal hemoglobin molecules. Thalassemia arises from an unbalanced hemoglobin chain synthesis of either the α or β protein, resulting in the underproduction of hemoglobin due to the inability to form sufficient quantities of hemoglobin heterotetramers.[9] Clinical presentation of thalassemia is extremely heterogeneous between patients in terms of clinical severity. However, three thalassemia subtypes have been described based on clinical severity, including thalassemia minor (usually asymptomatic and mild anemia), intermedia (microcytic anemia, hemolysis) and major (fatal in α-thalassemia, and requiring life-long transfusions in β-thalassemia).[195] The accumulation of globin-chain monomers underlies numerous changes in RBC properties, including increased intracellular viscosity, hydration and membrane rigidity.[196] These changes collectively contribute to changes in RBC deformability.

Sickle cell disease (SCD) is associated with β-hemoglobin (HBB) gene mutation that causes the normally biconcave RBC to assume a rigid, sickle-like shape.[197,198] This defect results in anemia and other acute sickling crisis events associated with vaso-occlusion, splenic sequestration and hemolysis of sickled RBCs.[199,200] It has been well-established that sickled RBCs are significantly less deformable than healthy cells, using methods such as ektacytometry,[14] micro-sieve filtration,[15,71] optical tweezers,[201] and atomic force microscopy.[92] However, only ~15% of RBC exhibit irreversible sickling[14,202] and there is a heterogeneous distribution of deformability in RBCs from individuals with SCD.[203] Conventional methods to measure RBC deformability fail to appreciate this heterogeneity either because they infer deformability from bulk RBC measurement or because they measure deformability of very few single cells. High throughput single cell deformability measurement could provide improved understanding of disease progression.

In both thalassemia and sickle cell diseases, choosing an appropriate clinical intervention is sometime arduous since there is no clear marker associated with disease state or severity.[204,205] However, RBC deformability has long been recognized as a putative biomechanical marker for clinical outcomes in thalassemia patients.[9–13] Similarly, RBC deformability decreases during acute vaso-occlusive events to cause pre-capillary obstruction.[197] Paradoxically, early studies

suggested that RBCs with increased deformability was associated with RBC adhesion-associated occlusion of blood vessels in SCD.[56,57] However, vaso-adhesion appears to be independent of RBC deformability since hydroxyurea therapy reduces the incidence of vaso-occlusion while increasing RBC deformability, as measured by micropipette and filtration methods,[206] oxygen gradient ektacytometry,[207] and laser-assisted optional rotational cell analyzer (LORCA).[62] A similar increase in RBC deformability has been observed following treatment with a new drug, Voxelotor (gbt440).[208] However, these measures reflect the mean deformability of the bulk RBC deformability. Emerging evidence suggests that in both SCD[203] and thalassemia,[209] the existence of poorly deformable RBC subpopulations may disproportionately contribute to disease pathology. Therefore, the use of a high throughput, high sensitivity, and highly repeatable device that is able to measure small changes in deformability and relevant RBC subpopulations are essential in the study of both thalassemia and SCD.

7.4 Diabetes mellitus

Diabetes is a serious metabolic imbalance characterized by hyperglycemia caused by a defect in insulin secretion (type 1) or insulin responsiveness (type 2).[210] This defect is responsible for secondary complications including heart disease, stroke and nephropathy.[211] Nephropathy, or kidney disease, dramatically reduces life expectancy[212] and increases risk for developing cardiovascular disease.[213] While the pathophysiology of diabetes complications remains unclear, it has been suggested that functional alterations in the microcirculation and the development of nephropathy are linked to decreased RBC deformability.[17–19] In diabetic patients, there was early impairment in red blood cell deformability in patients with normal renal function. Furthermore, progressive impairment in red blood cell deformability was associated with renal function loss in all patients regardless of whether they had diabetes or not. The deformability of RBC in diabetic patients that developed retinopathy was also significantly affected compared to healthy controls.[214,215] Therefore, the onset of diabetes, as well as complications resulting from metabolic disturbances due to diabetes could be potentially anticipated by routine RBC deformability analysis. Since the deformability of the entire population of RBCs seems to be affected by diabetes, high-throughput single cell measurement of RBC deformability is likely not required. However, since ektacytometry and filtration failed to detect any deformability change resulting from healthy patients,[216,217] a device with a greater sensitivity is required to analyze the blood sample of patients with diabetes.

8. Concluding remarks

Cell deformability is a critical characteristic of RBCs that enable them to transit through the smallest capillaries in the human body. Consequently, RBC deformability is a potential biomarker for the status of many diseases. Traditional methods for measuring RBC deformability faces major challenges associated with measuring minute forces required to deform individual RBCs, as well as measuring changes in deformability that occur in a small subpopulation of cells. Microfluidic technologies have been able to overcome these challenges, and now surpass traditional methods in terms of sensitivity, throughput, consistency, and ease-of-use. Recent advances in microfluidics now make it feasible to assess RBC deformability as a biomarker for malaria and hereditary hemoglobinopathies, as well as for evaluating quality of donated RBCs for use in blood transfusions.

Conflicts of interest

There are no conflicts to declare.

Acknowledgements

This work was supported by grants from the Canadian Institutes of Health Research (grant numbers: 322375, 362500, and 414861), Natural Sciences and Engineering Research Council of Canada (grant numbers: 538818-19 and 2015–06541), MITACS (grant number: IT09621 to KM).

References

1 J. M. Kwan, Q. Guo, D. L. Kyluik-Price, H. Ma and M. D. Scott, *Am. J. Hematol.*, 2013, **88**, 682–689.
2 H. A. del Portillo, M. Ferrer, T. Brugat, L. Martin-Jaular, J. Langhorne and M. V. G. Lacerda, *Cell. Microbiol.*, 2012, **14**, 343–355.
3 L. T. Chen and L. Weiss, *Blood*, 1973, **41**, 529–537.
4 L. Weiss and M. Tavassoli, *Semin. Hematol.*, 1970, **7**, 372–380.
5 Q. Guo, S. J. Reiling, P. Rohrbach and H. Ma, *Lab Chip*, 2012, **12**, 1143–1150.
6 J. P. Mills, L. Qie, M. Dao, K. S. W. Tan, C. T. Lim and S. Suresh, *MRS Online Proc. Libr.*, 2004, **844**, 179–184.
7 H. A. Cranston, C. W. Boylan, G. L. Carroll, S. P. Sutera, J. R. Williamson, I. Y. Gluzman and D. J. Krogstad, *Science*, 1984, **223**, 400–403.
8 G. B. Nash, E. O'Brien, E. C. Gordon-Smith and J. A. Dormandy, *Blood*, 1989, **74**, 855–861.
9 M. D. Scott, P. Rouyer-Fessard, M. S. Ba, B. H. Lubin and Y. Beuzard, *Br. J. Haematol.*, 1992, **80**, 519–526.
10 A. Vayá, J. Iborra, C. Falcó, I. Moreno, P. Bolufer, F. Ferrando, M. L. Pérez and J. Aznar, *Clin. Hemorheol. Microcirc.*, 2003, **28**, 71–78.
11 S. L. Schrier, E. Rachmilewitz and N. Mohandas, *Blood*, 1989, **74**, 2194–2202.
12 I. Dulińska, M. Targosz, W. Strojny, M. Lekka, P. Czuba, W. Balwierz and M. Szymoński, *J. Biochem. Biophys. Methods*, 2006, **66**, 1–11.
13 W. Tillmann and W. Schröter, *Br. J. Haematol.*, 1979, **43**, 401–411.

14 S. Chien, S. Usami and J. F. Bertles, *J. Clin. Invest.*, 1970, **49**, 623–634.
15 S. Usami, S. Chien and J. Bertles, *J. Lab. Clin. Med.*, 1975, **86**(2), 274–279.
16 M. M. Brandão, A. Fontes, M. L. Barjas-Castro, L. C. Barbosa, F. F. Costa, C. L. Cesar and S. T. O. Saad, *Eur. J. Haematol.*, 2003, **70**, 207–211.
17 C. D. Brown, H. S. Ghali, Z. Zhao, L. L. Thomas and E. A. Friedman, *Kidney Int.*, 2005, **67**, 295–300.
18 T. Kunt, S. Schneider, A. Pfützner, K. Goitum, M. Engelbach, B. Schauf, J. Beyer and T. Forst, *Diabetologia*, 1999, **42**, 465–471.
19 L. O. Simpson, *Nephron*, 1985, **39**, 344–351.
20 T. Wu, Q. Guo, H. Ma and J. J. Feng, *Theor. Appl. Mech. Lett.*, 2015, **5**, 227–230.
21 Z. Wen, T. Gao, Z. Yan, L. Song, H. Dou, D. Sun, Z. Lü, Y. Shi and H. Xiao, *Sci. China, Ser. C: Life Sci.*, 1998, **41**, 195–202.
22 O. K. Baskurt, M. R. Hardeman, M. Uyuklu, P. Ulker, M. Cengiz, N. Nemeth, S. Shin, T. Alexy and H. J. Meiselman, *Biorheology*, 2009, **46**, 251–264.
23 A. M. Dondorp, P. A. Kager, J. Vreeken and N. J. White, *Parasitol. Today*, 2000, **16**, 228–232.
24 H. L. Reid, A. J. Barnes, P. J. Lock, J. A. Dormandy and T. L. Dormandy, *J. Clin. Pathol.*, 1976, **29**, 855–858.
25 T. L. Berezina, S. B. Zaets, C. Morgan, C. R. Spillert, M. Kamiyama, Z. Spolarics, E. A. Deitch and G. W. Machiedo, *J. Surg. Res.*, 2002, **102**, 6–12.
26 R. Selvan, P. Parthasarathi, S. S. Iyengar, S. Ananthamurthy and S. Bhattacharya, *PLoS One*, 2019, **14**, e0226640.
27 M. Lekka, M. Fornal, G. Pyka-Fościak, K. Lebed, B. Wizner, T. Grodzicki and J. Styczeń, *Biorheology*, 2005, **42**, 307–317.
28 J. P. Mills, L. Qie, M. Dao, C. T. Lim and S. Suresh, *Mech. Chem. Biosyst.*, 2004, **1**, 169–180.
29 M. Dao, C. T. Lim and S. Suresh, *J. Mech. Phys. Solids*, 2003, **51**, 2259–2280.
30 S. Hénon, G. Lenormand, A. Richert and F. Gallet, *Biophys. J.*, 1999, **76**, 1145–1151.
31 E. Evans, N. Mohandas and A. Leung, *J. Clin. Invest.*, 1984, **73**, 477–488.
32 R. P. Hebbel, A. Leung and N. Mohandas, *Blood*, 1990, **76**, 1015–1020.
33 S. C. Gifford, M. G. Frank, J. Derganc, C. Gabel, R. H. Austin, T. Yoshida and M. W. Bitensky, *Biophys. J.*, 2003, **84**, 623–633.
34 T. Herricks, M. Antia and P. K. Rathod, *Cell. Microbiol.*, 2009, **11**, 1340–1353.
35 A. M. Forsyth, J. Wan, W. D. Ristenpart and H. A. Stone, *Microvasc. Res.*, 2010, **80**, 37–43.
36 K. Tsukada, E. Sekizuka, C. Oshio and H. Minamitani, *Microvasc. Res.*, 2001, **61**, 231–239.
37 L. Guillou, J. B. Dahl, J.-M. G. Lin, A. I. Barakat, J. Husson, S. J. Muller and S. Kumar, *Biophys. J.*, 2016, **111**, 2039–2050.
38 Y. Henon, G. J. Sheard and A. Fouras, *RSC Adv.*, 2014, **4**, 36079.
39 D. R. Gossett, H. T. K. Tse, S. A. Lee, Y. Ying, A. G. Lindgren, O. O. Yang, J. Rao, A. T. Clark and D. Di Carlo, *Proc. Natl. Acad. Sci. U. S. A. U. S. A.*, 2012, **109**, 7630–7635.
40 D. Bento, R. Rodrigues, V. Faustino, D. Pinho, C. Fernandes, A. Pereira, V. Garcia, J. Miranda and R. Lima, *Micromachines*, 2018, **9**, 151.
41 M. Abkarian, M. Faivre and H. A. Stone, *Proc. Natl. Acad. Sci. U. S. A. U. S. A.*, 2006, **103**, 538–542.
42 Y. Zheng, J. Nguyen, C. Wang and Y. Sun, *Lab Chip*, 2013, **13**, 3275–3283.
43 H. Bow, I. V. Pivkin, M. Diez-Silva, S. J. Goldfless, M. Dao, J. C. Niles, S. Suresh and J. Han, *Lab Chip*, 2011, **11**, 1065.
44 M. J. Rosenbluth, W. A. Lam and D. A. Fletcher, *Lab Chip*, 2008, **8**, 1062–1070.
45 Q. Guo, S. P. Duffy, K. Matthews, X. Deng, A. T. Santoso, E. Islamzada and H. Ma, *Lab Chip*, 2016, **16**, 645–654.
46 E. Islamzada, K. Matthews, Q. Guo, A. T. Santoso, S. P. Duffy, M. D. Scott and H. Ma, *Lab Chip*, 2020, **20**, 226–235.
47 S. Shin, J. X. Hou, J. S. Suh and M. Singh, *Clin. Hemorheol. Microcirc.*, 2007, **37**, 319–328.
48 N. L. Parrow, P.-C. Violet, H. Tu, J. Nichols, C. A. Pittman, C. Fitzhugh, R. E. Fleming, N. Mohandas, J. F. Tisdale and M. Levine, *J. Visualized Exp.*, 2018, 56910.
49 C. Renoux, M. Faivre, A. Bessaa, L. Da Costa, P. Joly, A. Gauthier and P. Connes, *Sci. Rep.*, 2019, **9**, 6771.
50 S. Yu. Nikitin, A. V. Priezzhev and A. E. Lugovtsov, *J. Quant. Spectrosc. Radiat. Transfer*, 2013, **121**, 1–8.
51 J. Stuart, *J. Clin. Pathol.*, 1985, **38**, 965–977.
52 A. M. Dondorp, M. Nyanoti, P. A. Kager, S. Mithwani, J. Vreeken and K. Marsh, *Trans. R. Soc. Trop. Med. Hyg.*, 2002, **96**, 282–286.
53 A. M. Dondorp, B. J. Angus, M. R. Hardeman, K. T. Chotivanich, K. Silamut, R. Ruangveerayuth, P. A. Kager, N. J. White and J. Vreeken, *Am. J. Trop. Med. Hyg.*, 1997, **57**, 507–511.
54 A. M. Dondorp, K. T. Chotivanich, S. Fucharoen, K. Silamut, J. Vreeken, P. A. Kager and N. J. White, *Br. J. Haematol.*, 1999, **105**, 505–508.
55 S. K. Ballas and N. Mohandas, *Microcirculation*, 2004, **11**, 209–225.
56 S. K. Ballas, J. Larner, E. D. Smith, S. Surrey, E. Schwartz and E. F. Rappaport, *Blood*, 1988, **72**, 1216–1223.
57 W. M. Lande, D. L. Andrews, M. R. Clark, N. V. Braham, D. M. Black, S. H. Embury and W. C. Mentzer, *Blood*, 1988, **72**, 2056–2059.
58 N. L. Parrow, H. Tu, J. Nichols, P.-C. Violet, C. A. Pittman, C. Fitzhugh, R. E. Fleming, N. Mohandas, J. F. Tisdale and M. Levine, *Blood Cells, Mol., Dis.*, 2017, **65**, 41–50.
59 S. Shin, Y.-H. Ku, J.-X. Ho, Y.-K. Kim, J.-S. Suh and M. Singh, *Clin. Hemorheol. Microcirc.*, 2007, **36**, 253–261.
60 R. T. Card, N. Mohandas and P. L. Mollison, *Br. J. Haematol.*, 1983, **53**, 237–240.
61 M. R. Hardeman, J. G. G. Dobbe and C. Ince, *Clin. Hemorheol. Microcirc.*, 2001, **25**, 1–11.
62 N. Lemonne, K. Charlot, X. Waltz, S. K. Ballas, Y. Lamarre, K. Lee, R. Hierso, C. Connes, M. Etienne-Julan, M. Romana and P. Connes, *Haematologica*, 2015, **100**, e383–e386.

63 M. A. E. Rab, B. A. Oirschot, J. Bos, T. H. Merkx, A. C. W. Wesel, O. Abdulmalik, M. K. Safo, B. A. Versluijs, M. E. Houwing, M. H. Cnossen, J. Riedl, R. E. G. Schutgens, G. Pasterkamp, M. Bartels, E. J. Beers and R. Wijk, *Am. J. Hematol.*, 2019, **94**, 575–584.
64 R. E. Ware, M. de Montalembert, L. Tshilolo and M. R. Abboud, *Lancet*, 2017, **390**, 311–323.
65 W. A. Eaton and H. F. Bunn, *Blood*, 2017, **129**, 2719–2726.
66 A. Paikari and V. A. Sheehan, *Br. J. Haematol.*, 2018, **180**, 189–200.
67 O. K. Baskurt, M. Uyuklu, P. Ulker, M. Cengiz, N. Nemeth, T. Alexy, S. Shin, M. R. Hardeman and H. J. Meiselman, *J. Biomed. Opt.*, 2011, **16**(11), 117006.
68 J. M. Sosa, N. D. Nielsen, S. M. Vignes, T. G. Chen and S. S. Shevkoplyas, *Clin. Hemorheol. Microcirc.*, 2014, **57**, 275–289.
69 M. P. Doyle, W. R. Galey and B. R. Walker, *J. Appl. Physiol.*, 1989, **67**, 2593–2599.
70 P. C. Buchan, *Br. J. Haematol.*, 1980, **45**, 97–105.
71 M. W. Kenny, M. Meakin, D. J. Worthington and J. Stuart, *Br. J. Haematol.*, 1981, **49**, 103–109.
72 S. S. Shevkoplyas, T. Yoshida, S. C. Gifford and M. W. Bitensky, *Lab Chip*, 2006, **6**, 914.
73 J. A. Chasis and S. B. Shohet, *Annu. Rev. Physiol.*, 1987, **49**, 237–248.
74 R. M. Hochmuth, *J. Biomech.*, 2000, **33**, 15–22.
75 J. Kim, H. Lee and S. Shin, *J. Cell. Biotechnol.*, 2015, **1**, 63–79.
76 E. A. Evans, *Biophys. J.*, 1983, **43**, 27–30.
77 J. Sleep, D. Wilson, R. Simmons and W. Gratzer, *Biophys. J.*, 1999, **77**, 3085–3095.
78 M. Puig-de-Morales-Marinkovic, K. T. Turner, J. P. Butler, J. J. Fredberg and S. Suresh, *Am. J. Physiol.*, 2007, **293**, 597–605.
79 Y. Kim, K. Kim and Y. Park, in *Blood Cell - An Overview of Studies in Hematology*, ed. T. Moschandreou, InTech, 2012.
80 A. Sinha, T. T. T. Chu, M. Dao and R. Chandramohanadas, *Sci. Rep.*, 2015, **5**, 9768.
81 G. Lenormand, S. Hénon, A. Richert, J. Siméon and F. Gallet, *Biophys. J.*, 2001, **81**, 43–56.
82 S. Suresh, J. Spatz, J. P. Mills, A. Micoulet, M. Dao, C. T. Lim, M. Beil and T. Seufferlein, *Acta Biomater.*, 2005, **1**, 15–30.
83 K. Bambardekar, A. K. Dharmadhikari, J. A. Dharmadhikari, D. Mathur and S. Sharma, *J. Biomed. Opt.*, 2008, **13**, 064021.
84 S. K. Mohanty, A. Uppal and P. K. Gupta, *Biotechnol. Lett.*, 2004, **26**, 971–974.
85 H. Byun, T. R. Hillman, J. M. Higgins, M. Diez-Silva, Z. Peng, M. Dao, R. R. Dasari, S. Suresh and Y. Park, *Acta Biomater.*, 2012, **8**, 4130–4138.
86 R. R. Huruta, M. L. Barjas-Castro, S. T. O. Saad, F. F. Costa, A. Fontes, L. C. Barbosa and C. L. Cesar, *Blood*, 1998, **92**, 2975–2977.
87 M. L. Barjas-Castro, M. M. Brandão, A. Fontes, F. F. Costa, C. L. Cesar and S. T. O. Saad, *Transfusion*, 2002, **42**, 1196–1199.
88 J. Lukose, M. N. G. Mohan, S. Shastry and S. Chidangil, *RSC Adv.*, 2019, **9**, 7878–7884.
89 B. R. Wood, P. Caspers, G. J. Puppels, S. Pandiancherri and D. McNaughton, *Anal. Bioanal. Chem.*, 2007, **387**, 1691–1703.
90 T. Avsievich, R. Zhu, A. Popov, A. Bykov and I. Meglinski, *Rev. Phys.*, 2020, **5**, 100043.
91 K. E. Bremmell, A. Evans and C. A. Prestidge, *Colloids Surf., B*, 2006, **50**, 43–48.
92 J. Maciaszek and G. Lykotrafitis, *J. Biomech.*, 2011, **44**, 657–661.
93 G. Ciasca, M. Papi, S. Di Claudio, M. Chiarpotto, V. Palmieri, G. Maulucci, G. Nocca, C. Rossi and M. De Spirito, *Nanoscale*, 2015, **7**, 17030–17037.
94 A. Abay, G. Simionato, R. Chachanidze, A. Bogdanova, L. Hertz, P. Bianchi, E. van den Akker, M. von Lindern, M. Leonetti, G. Minetti, C. Wagner and L. Kaestner, *Front. Physiol.*, 2019, **10**, 514.
95 X. Chen, L. Feng, H. Jin, S. Feng and Y. Yu, *Clin. Hemorheol. Microcirc.*, 2009, **43**, 241–249.
96 A. V. Buys, M.-J. Van Rooy, P. Soma, D. Van Papendorp, B. Lipinski and E. Pretorius, *Cardiovasc. Diabetol.*, 2013, **12**, 25.
97 N. Wang, J. P. Butler and D. E. Ingber, *Science*, 1993, **260**, 1124–1127.
98 F. Cverna and W. A. Woishnis, *Engineering plastics and composites*, Asm Intl, 1993.
99 M. Sepe, *Adv. Mater. Process.*, 1992, **141**, 32–35.
100 D. A. Fedosov, B. Caswell and G. E. Karniadakis, *Biophys. J.*, 2010, **98**, 2215–2225.
101 M. Marinkovic, M. Diez-Silva, I. Pantic, J. J. Fredberg, S. Suresh and J. P. Butler, *Am. J. Physiol.*, 2009, **296**, C59–C64.
102 L. Chen, V. Maybeck, A. Offenhäusser and H.-J. Krause, *Rev. Sci. Instrum.*, 2016, **87**, 064301.
103 B. Fabry, G. N. Maksym, J. P. Butler, M. Glogauer, D. Navajas, N. A. Taback, E. J. Millet and J. J. Fredberg, *Phys. Rev. E: Stat., Nonlinear, Soft Matter Phys.*, 2003, **68**, 041914.
104 B. Fabry, G. N. Maksym, J. P. Butler, M. Glogauer, D. Navajas and J. J. Fredberg, *Phys. Rev. Lett.*, 2001, **87**, 148102.
105 Y. Zhang, F. Wei, Y.-C. Poh, Q. Jia, J. Chen, J. Chen, J. Luo, W. Yao, W. Zhou, W. Huang, F. Yang, Y. Zhang and N. Wang, *Nat. Protoc.*, 2017, **12**, 1437–1450.
106 J. Chen, M. Abdelgawad, L. Yu, N. Shakiba, W.-Y. Chien, Z. Lu, W. R. Geddie, M. A. S. Jewett and Y. Sun, *J. Micromech. Microeng.*, 2011, **21**, 054012.
107 A. Amirouche, M. Faivre, J. F. Chateaux and R. Ferrigno, in *2017 39th Annual International Conference of the IEEE Engineering in Medicine and Biology Society (EMBC)*, 2017, pp. 3584–3587.
108 N. A. Nodargi, J. Kiendl, P. Bisegna, F. Caselli and L. De Lorenzis, *Comput. Methods Appl. Mech. Eng.*, 2018, **338**, 392–411.
109 H. Engelhardt, H. Gaub and E. Sackmann, *Nature*, 1984, **307**, 378–380.
110 Y. Qiang, J. Liu, M. Dao, S. Suresh and E. Du, *Proc. Natl. Acad. Sci. U. S. A.*, 2019, **116**, 19828–19834.

111 Y. Qiang, J. Liu and E. Du, *Micromachines*, 2018, **9**, 21.
112 Y. Qiang, J. Liu, F. Yang, D. Dieujuste and E. Du, *Sci. Rep.*, 2018, **8**, 10224.
113 E. Du, M. Dao and S. Suresh, *Extreme Mech. Lett.*, 2014, **1**, 35–41.
114 M. Musielak, *Clin. Hemorheol. Microcirc.*, 2009, **42**, 47–64.
115 G. M. Whitesides, *Nature*, 2006, **442**, 368–373.
116 M.-E. Myrand-Lapierre, X. Deng, R. R. Ang, K. Matthews, A. T. Santoso and H. Ma, *Lab Chip*, 2015, **15**, 159–167.
117 X. Deng, S. P. Duffy, M.-E. Myrand-Lapierre, K. Matthews, A. T. Santoso, Y.-L. Du, K. S. Ryan and H. Ma, *Malar. J.*, 2015, **14**, 428.
118 K. Matthews, M.-E. Myrand-Lapierre, R. R. Ang, S. P. Duffy, M. D. Scott and H. Ma, *J. Biomech.*, 2015, **48**, 4065–4072.
119 K. Matthews, S. P. Duffy, M.-E. Myrand-Lapierre, R. R. Ang, L. Li, M. D. Scott and H. Ma, *Integr. Biol.*, 2017, **9**, 519–528.
120 A. T. Santoso, X. Deng, J.-H. Lee, K. Matthews, S. P. Duffy, E. Islamzada, S. M. McFaul, M.-E. Myrand-Lapierre and H. Ma, *Lab Chip*, 2015, **15**, 4451–4460.
121 T. Go, H. Byeon and S. J. Lee, *Sci. Rep.*, 2017, **7**, 41162.
122 A. C. Rowat, J. Lammerding, H. Herrmann and U. Aebi, *BioEssays*, 2008, **30**, 226–236.
123 D. Di Carlo, *Lab Chip*, 2009, **9**, 3038.
124 D. Di Carlo, D. Irimia, R. G. Tompkins and M. Toner, *Proc. Natl. Acad. Sci. U. S. A.*, 2007, **104**, 18892–18897.
125 D. R. Gossett and D. D. Carlo, *Anal. Chem.*, 2009, **81**, 8459–8465.
126 A. M. Forsyth, J. Wan, P. D. Owrutsky, M. Abkarian and H. A. Stone, *Proc. Natl. Acad. Sci. U. S. A.*, 2011, **108**, 10986–10991.
127 Y. Man, D. Maji, R. An, S. P. Ahuja, J. A. Little, M. A. Suster, P. Mohseni and U. A. Gurkan, *Lab Chip*, 2021, **21**, 1036–1048.
128 J. Liu, Y. Qiang, O. Alvarez and E. Du, *ACS Sens.*, 2019, **4**, 1783–1790.
129 T. Xu, M. A. Lizarralde-Iragorri, J. Roman, R. Ghasemi, J.-P. Lefèvre, E. Martincic, V. Brousse, O. Français, W. El Nemer and B. Le Pioufle, *Sci. Rep.*, 2020, **10**, 9869.
130 Q. Guo, S. Park and H. Ma, *Lab Chip*, 2012, **12**, 2687–2695.
131 Q. Guo, S. P. Duffy, K. Matthews, A. T. Santoso, M. D. Scott and H. Ma, *J. Biomech.*, 2014, **47**, 1767–1776.
132 M. A. Unger, H.-P. Chou, T. Thorsen, A. Scherer and S. R. Quake, *Science*, 2000, **288**, 113–116.
133 M. B. Jiménez-Díaz, D. Ebert, Y. Salinas, A. Pradhan, A. M. Lehane, M.-E. Myrand-Lapierre, K. G. O'Loughlin, D. M. Shackleford, M. J. de Almeida, A. K. Carrillo, J. A. Clark, A. S. M. Dennis, J. Diep, X. Deng, S. Duffy, A. N. Endsley, G. Fedewa, W. A. Guiguemde, M. G. Gómez, G. Holbrook, J. Horst, C. C. Kim, J. Liu, M. C. S. Lee, A. Matheny, M. S. Martínez, G. Miller, A. Rodríguez-Alejandre, L. Sanz, M. Sigal, N. J. Spillman, P. D. Stein, Z. Wang, F. Zhu, D. Waterson, S. Knapp, A. Shelat, V. M. Avery, D. A. Fidock, F.-J. Gamo, S. A. Charman, J. C. Mirsalis, H. Ma, S. Ferrer, K. Kirk, I. Angulo-Barturen, D. E. Kyle, J. L. DeRisi, D. M. Floyd and R. K. Guy, *Proc. Natl. Acad. Sci. U. S. A.*, 2014, **111**, E5455–E5462.
134 R. M. Hochmuth, P. R. Worthy and E. A. Evans, *Biophys. J.*, 1979, **26**, 101–114.
135 S. Huang, A. Undisz, M. Diez-Silva, H. Bow, M. Dao and J. Han, *Integr. Biol.*, 2013, **5**, 414–422.
136 Q. Guo, S. M. McFaul and H. Ma, *Phys. Rev. E: Stat., Nonlinear, Soft Matter Phys.*, 2011, **83**, 051910.
137 S. M. McFaul, B. K. Lin and H. Ma, *Lab Chip*, 2012, **12**, 2369–2376.
138 E. Islamzada, K. Matthews, E. S. Lamoureux, S. P. Duffy, M. D. Scott and H. Ma, *EJHaem*, 2022, **3**, 63–71.
139 E. Islamzada, K. Matthews, E. Lamoureux, S. P. Duffy, M. D. Scott and H. Ma, *Transfusion*, 2022, **62**, 448–456.
140 S. K. Debnath and Y. Park, *Opt. Lett.*, 2011, **36**, 4677.
141 G. Popescu, Y. Park, W. Choi, R. R. Dasari, M. S. Feld and K. Badizadegan, *Blood Cells, Mol., Dis.*, 2008, **41**, 10–16.
142 Y. Park, C. A. Best, T. Kuriabova, M. L. Henle, M. S. Feld, A. J. Levine and G. Popescu, *Phys. Rev. E: Stat., Nonlinear, Soft Matter Phys.*, 2011, **83**, 051925.
143 G. Popescu, T. Ikeda, C. A. Best, K. Badizadegan, R. R. Dasari and M. S. Feld, *J. Biomed. Opt.*, 2005, **10**, 060503.
144 Y. Park, C. A. Best, T. Auth, N. S. Gov, S. A. Safran, G. Popescu, S. Suresh and M. S. Feld, *Proc. Natl. Acad. Sci. U. S. A.*, 2010, **107**, 1289–1294.
145 R. Waugh and E. A. Evans, *Biophys. J.*, 1979, **26**, 115–131.
146 B. Bhaduri, C. Edwards, H. Pham, R. Zhou, T. H. Nguyen, L. L. Goddard and G. Popescu, *Adv. Opt. Photonics*, 2014, **6**, 57.
147 G. Popescu, T. Ikeda, R. R. Dasari and M. S. Feld, *Opt. Lett.*, 2006, **31**, 775–777.
148 Y. Wang, J. Sang, R. Ao, Y. Ma and B. Fu, *Comput. Methods Biomech. Biomed. Engin.*, 2020, **23**, 1190–1200.
149 J. Sun, A. Tárnok and X. Su, *Cytometry, Part A*, 2020, **97**, 226–240.
150 R. N. Pinto, J. A. Sebastian, M. J. Parsons, T. C. Chang, T. R. Turner, J. P. Acker and M. C. Kolios, *Cytometry, Part A*, 2019, **95**, 976–984.
151 M. Doan, J. A. Sebastian, J. C. Caicedo, S. Siegert, A. Roch, T. R. Turner, O. Mykhailova, R. N. Pinto, C. McQuin, A. Goodman, M. J. Parsons, O. Wolkenhauer, H. Hennig, S. Singh, A. Wilson, J. P. Acker, P. Rees, M. C. Kolios and A. E. Carpenter, *Proc. Natl. Acad. Sci. U. S. A.*, 2020, **117**, 21381–21390.
152 E. S. Lamoureux, E. Islamzada, M. V. J. Wiens, K. Matthews, S. P. Duffy and H. Ma, *Lab Chip*, 2022, **22**(1), 26–39.
153 J. A. Sebastian, M. C. Kolios and J. P. Acker, *Transfus. Apher. Sci.*, 2020, **59**, 103020.
154 M. Komorowska, M. Koter, G. Bartosz and J. Gomułkiewicz, *Biochim. Biophys. Acta*, 1982, **686**, 94–98.
155 T. L. Steck, *J. Mol. Biol.*, 1972, **66**, 295–305.
156 S. C. Gifford, J. Derganc, S. S. Shevkoplyas, T. Yoshida and M. W. Bitensky, *Br. J. Haematol.*, 2006, **135**, 395–404.
157 J. L. Carson, *Ann. Intern. Med.*, 2012, **157**, 49.
158 L. M. Napolitano, S. Kurek, F. A. Luchette, H. L. Corwin, P. S. Barie, S. A. Tisherman, P. C. Hebert, G. L. Anderson, M. R. Bard, W. Bromberg, W. C. Chiu, M. D. Cipolle, K. D. Clancy, L. Diebel, W. S. Hoff, K. M. Hughes, I. Munshi, D. Nayduch, R. Sandhu and J. A. Yelon, *Crit. Care Med.*, 2009, **37**, 3124–3157.

159 K. S. Gill, P. Muntner, R. A. Lafayette, J. Petersen, J. C. Fink, D. T. Gilbertson and B. D. Bradbury, *Nephrol., Dial., Transplant.*, 2013, **28**, 1504–1515.
160 E. J. Werner, *Pediatr. Clin. North Am.*, 1996, **43**, 683–707.
161 G. M. Clarke and T. N. Higgins, *Clin. Chem.*, 2000, **46**, 1284–1290.
162 P. J. Barrett-Lee, N. P. Bailey, M. E. O'Brien and E. Wager, *Br. J. Cancer*, 2000, **82**, 93–97.
163 S. J. Wagner, *Vox Sang.*, 2004, **86**, 157–163.
164 J. E. Hendrickson and C. D. Hillyer, *Anesth. Analg.*, 2009, **108**, 759–769.
165 J. Bux, *Vox Sang.*, 2005, **89**, 1–10.
166 C. F. Högman and H. T. Meryman, *Transfusion*, 2006, **46**, 137–142.
167 A. D'Alessandro, G. Liumbruno, G. Grazzini and L. Zolla, *J. Geophys. Res. Space Physics*, 2010, **8**, 82–88.
168 K. Pavenski, E. Saidenberg, M. Lavoie, M. Tokessy and D. R. Branch, *Transfus. Med. Rev.*, 2012, **26**, 68–84.
169 V. L. Tzounakas, A. G. Kriebardis, I. S. Papassideri and M. H. Antonelou, *Proteomics: Clin. Appl.*, 2016, **10**, 791–804.
170 D. Unruh, R. Srinivasan, T. Benson, S. Haigh, D. Coyle, N. Batra, R. Keil, R. Sturm, V. Blanco, M. Palascak, R. S. Franco, W. Tong, T. Chatterjee, D. Y. Hui, W. S. Davidson, B. J. Aronow, T. Kalfa, D. Manka, A. Peairs, A. Blomkalns, D. J. Fulton, J. E. Brittain, N. L. Weintraub and V. Y. Bogdanov, *Circulation*, 2015, **132**, 1898–1908.
171 M. del M. Romero, J. A. Fernández-López, X. Remesar and M. Alemany, *PLoS One*, 2012, **7**, e34381.
172 R. L. Sparrow, *Blood Transfus.*, 2017, **15**(2), 116–125.
173 E. Bennett-Guerrero, T. H. Veldman, A. Doctor, M. J. Telen, T. L. Ortel, T. S. Reid, M. A. Mulherin, H. Zhu, R. D. Buck, R. M. Califf and T. J. McMahon, *Proc. Natl. Acad. Sci. U. S. A. U. S. A.*, 2007, **104**, 17063–17068.
174 V. Nagaprasad and M. Singh, *Clin. Hemorheol. Microcirc.*, 1998, **18**, 273–284.
175 G. Barshtein, T. L. Rasmusen, O. Zelig, D. Arbell and S. Yedgar, *Transfus. Med.*, 2020, **30**, 492–496.
176 M. Chassé, L. McIntyre, S. W. English, A. Tinmouth, G. Knoll, D. Wolfe, K. Wilson, N. Shehata, A. Forster, C. van Walraven and D. A. Fergusson, *Transfus. Med. Rev.*, 2016, **30**, 69–80.
177 N. M. Heddle, R. J. Cook, Y. Liu, M. Zeller, R. Barty, J. P. Acker, J. Eikelboom and D. M. Arnold, *Transfusion*, 2019, **59**, 482–491.
178 WHO Team, Global malaria programme, *World malaria report 2020*, https://www.who.int/publications-detail-redirect/9789240015791, (accessed October 12, 2021).
179 T. N. C. Wells, P. L. Alonso and W. E. Gutteridge, *Nat. Rev. Drug Discovery*, 2009, **8**, 879–891.
180 Z. Bozdech, M. Llinás, B. L. Pulliam, E. D. Wong, J. Zhu and J. L. DeRisi, *PLoS Biol.*, 2003, **1**, e5.
181 X. Su, V. M. Heatwole, S. P. Wertheimer, F. Guinet, J. A. Herrfeldt, D. S. Peterson, J. A. Ravetch and T. E. Wellems, *Cell*, 1995, **82**, 89–100.
182 C. L. Mackintosh, J. G. Beeson and K. Marsh, *Trends Parasitol.*, 2004, **20**, 597–603.
183 F. K. Glenister, R. L. Coppel, A. F. Cowman, N. Mohandas and B. M. Cooke, *Blood*, 2002, **99**, 1060–1063.
184 B. M. Cooke, N. Mohandas and R. L. Coppel, *Adv. Parasitol.*, 2001, **50**, 1–86.
185 A. G. Maier, M. Rug, M. T. O'Neill, M. Brown, S. Chakravorty, T. Szestak, J. Chesson, Y. Wu, K. Hughes, R. L. Coppel, C. Newbold, J. G. Beeson, A. Craig, B. S. Crabb and A. F. Cowman, *Cell*, 2008, **134**, 48–61.
186 F. Nuchsongsin, K. Chotivanich, P. Charunwatthana, O. S. Fausta, D. Taramelli, N. P. Day, N. J. White and A. M. Dondorp, *Am. J. Trop. Med. Hyg.*, 2007, **77**, 617–622.
187 F. Omodeo-Salè, A. Motti, N. Basilico, S. Parapini, P. Olliaro and D. Taramelli, *Blood*, 2003, **102**, 705–711.
188 J. Combrinck, T. Mabotha, K. Ncokazi, M. Ambele, D. Taylor, P. Smith, H. Hoppe and T. Egan, *ACS Chem. Biol.*, 2013, **8**(1), 133–137.
189 M. Diez-Silva, M. Dao, J. Han, C.-T. Lim and S. Suresh, *MRS Bull.*, 2010, **35**, 382–388.
190 J. Stuart and G. B. Nash, *Blood Rev.*, 1990, **4**, 141–147.
191 F. C. Mokken, M. Kedaria, C. P. Henny, M. R. Hardeman and A. W. Gelb, *Ann. Hematol.*, 1992, **64**, 113–122.
192 S. Huang, A. Amaladoss, M. Liu, H. Chen, R. Zhang, P. R. Preiser, M. Dao and J. Han, *Infect. Immun.*, 2014, **82**, 2532–2541.
193 K. Chotivanich, R. Udomsangpetch, A. Dondorp, T. Williams, B. Angus, J. A. Simpson, S. Pukrittayakamee, S. Looareesuwan, C. I. Newbold and N. J. White, *J. Infect. Dis.*, 2000, **182**, 629–633.
194 A. T. Santoso, X. Deng, J.-H. Lee, K. Matthews, S. P. Duffy, E. Islamzada, S. M. McFaul, M.-E. Myrand-Lapierre and H. Ma, *Lab Chip*, 2015, **15**(23), 4451–4460.
195 D. R. Higgs, J. D. Engel and G. Stamatoyannopoulos, *Lancet*, 2012, **379**, 373–383.
196 S. L. Schrier M. D., *Annu. Rev. Med.*, 1994, **45**, 211–218.
197 D. C. Rees, T. N. Williams and M. T. Gladwin, *Lancet*, 2010, **376**, 2018–2031.
198 M. Stuart and R. Nagel, *Lancet*, 2004, **364**(9442), 1343–1360.
199 A. M. Emond, R. Collis, D. Darvill, D. R. Higgs, G. H. Maude and G. R. Serjeant, *J. Pediatr.*, 1985, **107**, 201–206.
200 J. M. Topley, D. W. Rogers, M. C. Stevens and G. R. Serjeant, *Arch. Dis. Child.*, 1981, **56**, 765–769.
201 M. M. Brandão, A. Fontes, M. L. Barjas-Castro, L. C. Barbosa, F. F. Costa, C. L. Cesar and S. T. O. Saad, *Eur. J. Haematol.*, 2003, **70**, 207–211.
202 D. K. Kaul, M. E. Fabry, P. Windisch, S. Baez and R. L. Nagel, *J. Clin. Invest.*, 1983, **72**, 22–31.
203 Y. Alapan, J. A. Little and U. A. Gurkan, *Sci. Rep.*, 2014, **4**, 7173.
204 D. K. Wood, A. Soriano, L. Mahadevan, J. M. Higgins and S. N. Bhatia, *Sci. Transl. Med.*, 2012, **4**, 123ra26.
205 A. Taher, H. Isma'eel and M. D. Cappellini, *Blood Cells, Mol., Dis.*, 2006, **37**, 12–20.
206 G. Athanassiou, A. Moutzouri, A. Kourakli and N. Zoumbos, *Clin. Hemorheol. Microcirc.*, 2006, **35**, 291–295.
207 A. Sadaf, K. G. Seu, E. Thaman, R. Fessler, D. G. Konstantinidis, H. A. Bonar, J. Korpik, R. E. Ware, P. T. McGann, C. T. Quinn and T. A. Kalfa, *Front. Physiol.*, 2021, **12**, 389.

208 K. Dufu, M. Patel, D. Oksenberg and P. Cabrales, *Clin. Hemorheol. Microcirc.*, 2018, **70**, 95–105.
209 P. Guruprasad, R. G. Mannino, C. Caruso, H. Zhang, C. D. Josephson, J. D. Roback and W. A. Lam, *Am. J. Hematol.*, 2019, **94**, 189–199.
210 American Diabetes Association, *Diabetes Care*, 2014, **37**, S81–S90.
211 M. A. Bush, *Am. J. Manag. Care*, 2010, **16**, S304–S307.
212 E. Ritz and S. R. Orth, *N. Engl. J. Med.*, 1999, **341**, 1127–1133.
213 J. M. Forbes and M. E. Cooper, *Physiol. Rev.*, 2013, **93**, 137–188.
214 R. Agrawal, T. Smart, J. Nobre-Cardoso, C. Richards, R. Bhatnagar, A. Tufail, D. Shima, P. H. Jones and C. Pavesio, *Sci. Rep.*, 2016, **6**, 15873.
215 E. J. Diamantopoulos, S. A. Raptis and S. D. Moulopoulos, *Horm. Metab. Res.*, 1987, **19**, 569–573.
216 J. R. Williamson, R. A. Gardner, C. W. Boylan, G. L. Carroll, K. Chang, J. S. Marvel, B. Gonen, C. Kilo, R. Tran-Son-Tay and S. P. Sutera, *Blood*, 1985, **65**, 283–288.
217 N. H. Schut, E. C. van Arkel, M. R. Hardeman, H. J. G. Bilo, R. P. J. Michels and J. Vreeken, *Acta Diabetol.*, 1993, **30**, 89–92.